



Photo-Fenton degradation of tetracycline over Z-scheme Fe-g-C₃N₄/Bi₂WO₆ heterojunctions: Mechanism insight, degradation pathways and DFT calculation

Caihua Liu^a, Hongling Dai^a, Chaoqun Tan^b, Qianyu Pan^a, Fengping Hu^a, Xiaoming Peng^{a,*}

^a School of Civil Engineering and Architecture, East China Jiaotong University, Nanchang 330013, Jiangxi Province, China

^b Department of Municipal Engineering, Southeast University, Nanjing, China

ARTICLE INFO

Keywords:

Z-scheme heterojunctions

DFT theoretical

Fe-N₄ sites

Spin state

Degradation

ABSTRACT

Herein, Fe-g-C₃N₄/Bi₂WO₆ Z-scheme heterojunction is elaborately designed to build a photo-Fenton system for the degradation of tetracycline (TC). In this study, the H₂O₂ decomposition performance of the Z-scheme heterojunction has been improved due to the doping of iron, improve photogenerated electrons transportability and facilitate spread of radicals, according to the efficacy analyses, and trapping experiment, ESR analysis as well as degradation pathways of TC. Moreover, DFT theoretical results suggest that the Z-scheme transfer route coupled with the generated photo-Fenton process builds a Z-scheme-charge-transfer platform for remarkable degradation of emerging pollutants, and the formation of Fe-N₄ sites induces a spin polarization of the material and also introduces a defect state in the original forbidden band, which leads to extremely activity for the removal of TC in the photo-Fenton system. The study shows that ¹O₂ and •O₂⁻ are the main active species participating in the degradation process.

1. Introduction

The use of antibiotics in treating human and animal infections has increased dramatically in the past few decades in response to climate change, population growth, pollution, and rapid economic development [1–4]. The tetracycline (TC), which is a typical antibiotic, has been widely used in human therapy, animal treatment, and agricultural production. It is reported that the annual about 210,000 tons of TC was discharged into the aquatic environment together with wastewater during the last few decades [5–11]. Moreover, the Chinese Academy of Sciences (CAS) has revealed in its reports that TC has been found in various waterways like, groundwater, surface water, and even drinking water, which constitutes a severe threat to the environment and human health. Therefore, the TC removal from the aquatic environment has become a mandatory requirement. However, On the other hand, TC cannot be effectively removed by traditional wastewater treatment techniques due to their strong chemical structure and strong resistance to biodegradation [12–16]. Consequently, there is an urgent need for more effective methods to eliminate TC pollutants.

Advanced oxidation processes (AOPs) are the common methods to treat organic pollutants in water because they can efficiently generate

highly active free oxygen radicals (ROS) to attack and degrade target organic pollutants efficiently. Among all the advanced oxidation processes, the photo-Fenton reaction is more frequently used to degrade of various organic contaminants due to its low cost, simplicity of operation, mild reaction conditions, and high efficiency [17–22]. Nonetheless, the traditional photo-Fenton reaction still has some inadequacies that limit its practical applications, such as the low photogenerated electron concentration and poor recyclability, that will result in relatively low efficiency of Fe³⁺/Fe²⁺ translation, as well as the limit in the efficient activation of H₂O₂, thus significantly increasing production costs and producing a mass of iron-containing waste after the reaction [23,24]. As an efficient way to address these challenges, photo-Fenton technology based on the construction of the Z-scheme system has gained increasing attention in recent years as a result of its oxidation capacity, and the capability of restraining the interface recombination of photo-excited charge carriers to form Z-scheme heterojunction. Recent studies have shown that introducing a valence transition metal to Z-scheme heterojunction is a novel and effective technique to improve its photocatalytic activity. In addition, many researchers have also demonstrated that a high concentration of photogenerated electrons can facilitate Fe³⁺/Fe²⁺ cycling and increase the ionization efficiency of H₂O₂ in the

* Corresponding author.

E-mail address: pengxiaoming70@ecjtu.edu.cn (X. Peng).

<https://doi.org/10.1016/j.apcatb.2022.121326>

Received 11 December 2021; Received in revised form 21 February 2022; Accepted 14 March 2022

Available online 16 March 2022

0926-3373/© 2022 Elsevier B.V. All rights reserved.

photo-Fenton system [25–31]. In other words, Fe-species heterogeneous Fenton catalysts have been proven to be an excellent candidate for constructing Z-scheme photocatalytic heterojunction systems, which can preserve more photocatalytic and Fenton-like metal sites so as to exhibit excellent catalytic activity in H_2O_2 activation and generate a potent oxidant hydroxyl radical ($\bullet\text{OH}$). Moreover, the Fe-doped Z-scheme system has enhanced the electron transfer, which leads to effective H_2O_2 utilization and better catalytic performance [32]. Meanwhile, the combination of Fe-species and Z-scheme heterojunction can also boost photo-Fenton catalytic activity, which benefits from the synergistic effect between iron ($\text{Fe}^{3+}/\text{Fe}^{2+}$) based Fenton and Z-scheme heterojunction photocatalytic process. It's another available key in reducing iron-containing sludge accumulation, which helps ensure that the synergy system can enhance the utilization efficiency of Z-scheme heterojunction.

In this study, the Z-scheme heterojunction photocatalysts of Fe-g-C₃N₄ and Bi₂WO₆ have been combined to achieve efficient degradation of TC. In addition, Fe-species have been anchored in g-C₃N₄ in the form of Fe-N₄ sites, and applied to the photo-Fenton process, which can contribute to the activation of H_2O_2 and then the removal of organic pollutants. Meanwhile, a possible photocatalytic performance of TC degradation by activating H_2O_2 over Z-scheme Fe-g-C₃N₄/Bi₂WO₆ heterojunction under the irradiation of simulated visible light in the photo-Fenton system have been evaluated by analyzing the morphological structure, optical techniques, and electrochemical impedance spectroscopy. Furthermore, the pathway and possible mechanism for catalytic oxidation have been proposed based on the capture experiment, H_2O_2 consumption, Density functional theory (DFT), and LC-MS. This study is expected to provide a newly cost-effective photo-Fenton-like activation approach and illustrate the possibility of applying Z-scheme heterojunction in photo-Fenton reactions for environmental treatment.

2. Materials and methods

2.1. Materials

Melamine, iron nitrate nonahydrate ($\text{Fe}(\text{NO}_3)_3 \cdot 9\text{H}_2\text{O}$), sodium tungstate dihydrate ($\text{Na}_2\text{WO}_4 \cdot 2\text{H}_2\text{O}$), Bismuth nitrate pentahydrate ($\text{Bi}(\text{NO}_3)_3 \cdot 5\text{H}_2\text{O}$), NaOH, HNO_3 , H_2O_2 , tetracycline (TC), ciprofloxacin (CIP), norfloxacin (NOX), ofloxacin (OFX), methylene blue (MB), humic acid (HA), ethylenediaminetetraacetic acid disodium salt (EDTA-2Na), Hexachloroethane, furfuryl alcohol (FFA), tert-Butanol (TBA), ethanol, oxalate, Sodium hydrosulfide (NaSCN), KI, potassium hydrogen phthalate ($\text{C}_8\text{H}_5\text{KO}_4$), NaCl, Na_2CO_3 , NaNO_3 , NaH_2PO_4 , and methyl alcohol (MeOH) were procured from Shanghai Macklin Biochemical Co., Ltd, while deionized water used to prepare the solution was extracted from the Milli-Q purification system.

2.2. Synthesis of the samples

2.2.1. Synthesis of Fe-g-C₃N₄ (Fe-CN)

The Fe-doped g-C₃N₄ material was synthesized in accordance with an approach proposed in a previous report. The preparation process is as follows: a certain amount of melamine was weighed into the crucible, which then was placed in a box-type resistance furnace with the temperature raised to 550 °C at a heating rate of 5 °C/min and calcined for 4 h. After it cooled to room temperature, the g-C₃N₄ powder was obtained. Then 0.02 g, 0.04 g, and 0.08 g of $\text{Fe}(\text{NO}_3)_3 \cdot 9\text{H}_2\text{O}$ were dissolved in 30 mL of deionized water separately with 4 g of melamine powder and the mixture was continuously stirred for 0.5 h. Afterward, it was heated to 60 °C to evaporate the water, and the resulting solid was then dried in an oven at 90 °C for 6 h. At last, the final products were transferred into a crucible and heated with the temperature rising to 550 °C at a rate of 5 °C/min before they were calcined for 2 h. As it cooled, Fe-doped g-C₃N₄ (Fe-g-C₃N₄) was obtained. For comparison, the samples with different content of Fe ions, which correspond to g-C₃N₄ (0 g), 0.5Fe-CN

(0.02 g), 1Fe-CN (0.04 g), and 2Fe-CN (0.08 g), have been prepared too. Fe-g-C₃N₄ is generally 2Fe-CN if not otherwise specified in this paper.

2.2.2. Synthesis of Fe-g-C₃N₄/Bi₂WO₆ (Fe-CN/BWO)

Briefly, 0.97 g of $\text{Bi}(\text{NO}_3)_3 \cdot 5\text{H}_2\text{O}$ and a certain amount of Fe-g-C₃N₄ were evenly dispersed into 60 mL of 0.4 M HNO_3 by ultrasonic for 10 min and were stirred for 20 min. Then 20 mL of 0.05 M $\text{Na}_2\text{WO}_4 \cdot 2\text{H}_2\text{O}$ was added dropwise, and the mixture was evenly stirred for 30 min. The mixed suspension was then transferred to a polytetrafluoroethylene-lined high-pressure reactor and heated at 170 °C for 18 h. After the resulting sample was centrifuged and cleaned in deionized water and ethanol several times, the obtained powder was dried in a vacuum drying oven at 70 °C for 10 h to gain Fe-g-C₃N₄/Bi₂WO₆ (0.5Fe-CN/BWO, 1Fe-CN/BWO and 2Fe-CN/BWO) composites. To prepare Bi₂WO₆ material, the above experimental steps have been repeated without Fe-g-C₃N₄ material. Fe-CN/BWO refers to 2Fe-CN/BWO if not otherwise specified in this paper. The characterization methods for the preparation of the sample catalysts are described in detail in the [Supplementary Information](#).

3. Results and discussion

3.1. Characterizations of the samples

The XRD patterns of the g-C₃N₄, Fe-g-C₃N₄, Bi₂WO₆, 1Fe-CN/BWO, and 2Fe-CN/BWO photocatalysts are displayed in Fig. 1a. The interfacial stackings of the conjugate construction and the heptazine network, have two distinct peaks at 13.0° and 27.4° in the (100) and (002) planes of g-C₃N₄ and Fe-g-C₃N₄, respectively [33,34]. No peaks of iron species can be observed in the XRD of the Fe-g-C₃N₄ catalyst, indicating that the loaded iron is most likely highly dispersed on g-C₃N₄ in the form of Fe-N_x bonds [35]. As shown in Fig. 1a, prominent diffraction peaks of the samples can be observed at 28.30°, 32.91°, 47.14°, 55.99°, 58.54°, 69.04°, 76.08°, and 78.53°, which respectively correspond to (131), (002), (202), (133), (262), (083), (2102) and (204) planes of the orthogonal crystal system of Bi₂WO₆ (JCPDS NO. 39-0256) [36,37]. The characteristic peaks of Fe-g-C₃N₄ could not be seen in the Fe-CN/BWO samples due to the low crystallinity of Fe-g-C₃N₄ and the overlap of the characteristic peaks of Fe-g-C₃N₄ and Bi₂WO₆ at 27.4° [38]. The results of FTIR and SEM analysis jointly confirm that Fe-CN/BWO has been successfully synthesized.

The FTIR spectrum of the prepared sample is shown in Fig. 1b with, the peak at about 810 cm^{-1} due to the breathing pattern of the g-C₃N₄ triazine unit. The peaks in the absorption band in the range of 1200–1750 cm^{-1} belong to the vibrational stretching mode of the aromatic C-N bond. The broadband center at about 3150 cm^{-1} might be attributed to the stretching pattern of the N-H bond. At 400–800 cm^{-1} , the pure Bi₂WO₆ sample shows a bridge stretching pattern to the W-O, Bi-O, and W-O-W bonds. In addition, all the characteristic absorption bands of Fe-g-C₃N₄ and Bi₂WO₆ appear in the spectra of the Fe-CN/BWO composites, suggesting that the Fe-g-C₃N₄ has been successfully loaded onto Bi₂WO₆ composites and no structural changes have occurred during the compounding process [39].

X-ray absorption near edge structure (XANES) and extended X-ray absorption fine spectroscopy (EXAFS) were further used to clarify the coordination information of Fe species in Fe-g-C₃N₄. As shown in Fig. 1c, the K-edge XANES spectral energy absorption edge of Fe in sample Fe-g-C₃N₄ is located between Fe foil and Fe₂O₃, which indicated that Fe in sample Fe-g-C₃N₄ has a positive charge between Fe⁰ and Fe³⁺ [40–43]. The FT K³ weighted $\chi(k)$ The function EXAFS spectrum (Fig. 1d) of Fe-g-C₃N₄ displayed that the Fe-g-C₃N₄ catalyst showed a dominant peak at 1.4 Å at the Fe K-edge, which can be attributed to the Fe-N coordination. According to quantitative EXAFS fitting (Table S1), the Fe-N coordination of Fe-g-C₃N₄ was determined to be 4.2. In addition, the WT contour map of Fe-g-C₃N₄ showed a maximum intensity of about 4.0 Å⁻¹ (Fig. 1f). In order to obtain the quantitative structural parameters of Fe

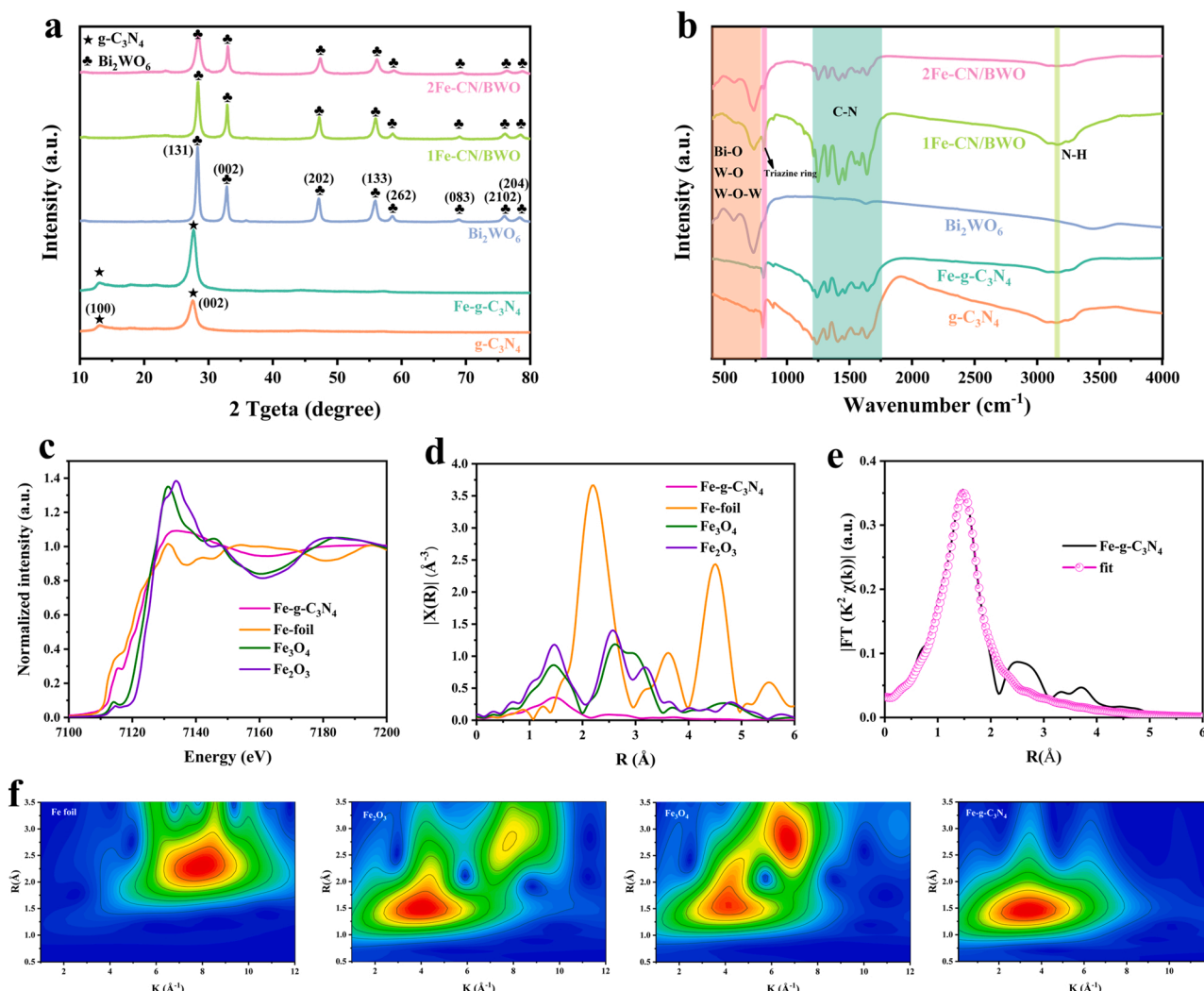


Fig. 1. (a) XRD and (b) FTIR patterns of the prepared sample, (c) Fe K-edge spectra of Fe-g-C₃N₄ and its reference (Fe foil, Fe₃O₄, and Fe₂O₃), (d) FT k³-weighted EXAFS spectra of Fe-g-C₃N₄ and its reference, (e) The EXAFS R space fitting curves of Fe-g-C₃N₄ and (f) Wavelet transformed (WT) EXAFS of Fe-g-C₃N₄ and its references.

in Fe-g-C₃N₄ catalyst, the least square EXAFS curve fitting was carried out (Fig. 1e). The results showed that the coordination number of Fe-N_x in Fe-g-C₃N₄ catalyst was about 4.

The geomorphology of the prepared photocatalysts has been analyzed by SEM images. As shown in Fig. S2c-d, the microscopic morphology of Fe-g-C₃N₄ is similar to the lamellar structure of g-C₃N₄ (Fig. S2a-b), demonstrating that the doped Fe did not alter the lamellar structure of g-C₃N₄ [44]. From Fig. S2e-f, pure Bi₂WO₆ is composed of many two-dimensional nanosheets of a thickness of 20–50 nm with petal-like microspheres. As shown in Fig. S2g-h, the Fe-CN/BWO composite decorated by Fe-g-C₃N₄ presents an agglomerated petal shape similar to that of pure Bi₂WO₆ [37]. It implies that Fe-g-C₃N₄ is well compounded with Bi₂WO₆, which agrees with the previous XRD and FTIR results. All these results reveal that Fe-g-C₃N₄ has been finely decentralized on the surface of Bi₂WO₆. Furthermore, the specific surface areas of Fe-g-C₃N₄ and Fe-CN/BWO in Fig. S3 are 25.536 m²/g and 35.195 m²/g with the pore sizes as 3.060 nm and 3.419 nm, respectively. It shows that the complexation of Fe-g-C₃N₄ with petaloid Bi₂WO₆ can improve the physicochemical characteristics to increase the specific surface area and pore size, thus accelerating the separation of photogenerated carriers and providing more reactive sites for catalytic degradation reactions.

3.2. Optical properties of the samples

In this paper, the optical properties of all samples have been studied through UV–vis diffuse reflectance spectroscopy (UV–vis DRS). In Fig. 2a, the absorption edge of Fe-CN/BWO increases significantly as the Fe-g-C₃N₄ is loaded onto Bi₂WO₆, indicating that the Z-scheme photo-Fenton catalysts can be constructed to facilitate the absorption of light to form more active species for effective photocatalytic activity. In Fig. 2b, the bandgap (E_g) of these samples can be estimated by the following equation [45].

$$(\alpha h\nu) = A(h\nu - E_g)^{\frac{2}{3}} \quad (1)$$

The absorption coefficient, Planck's constant, optical frequency (Hz), a constant, and bandgap energy are represented by α , h , ν , A , and E_g , respectively, while the n is determined by the type of optical leap in the material. The n is 1 for direct bandgap semiconductors and 4 for indirect bandgap semiconductors [46]. As the n value of g-C₃N₄, Fe-g-C₃N₄ and Bi₂WO₆ all are 1, the estimated E_g values for g-C₃N₄, Fe-g-C₃N₄, and Bi₂WO₆ are 2.77 eV, 2.80 eV, and 2.80 eV, respectively, which are consistent with those reported in other studies [47–49]. The estimated E_g values of 0.5Fe-CN/BWO, 1Fe-CN/BWO and 2Fe-CN/BWO are 2.92 eV, 2.86 eV and 2.78 eV respectively. With the increase of Fe content in the sample, the band gap of the sample also decreases,

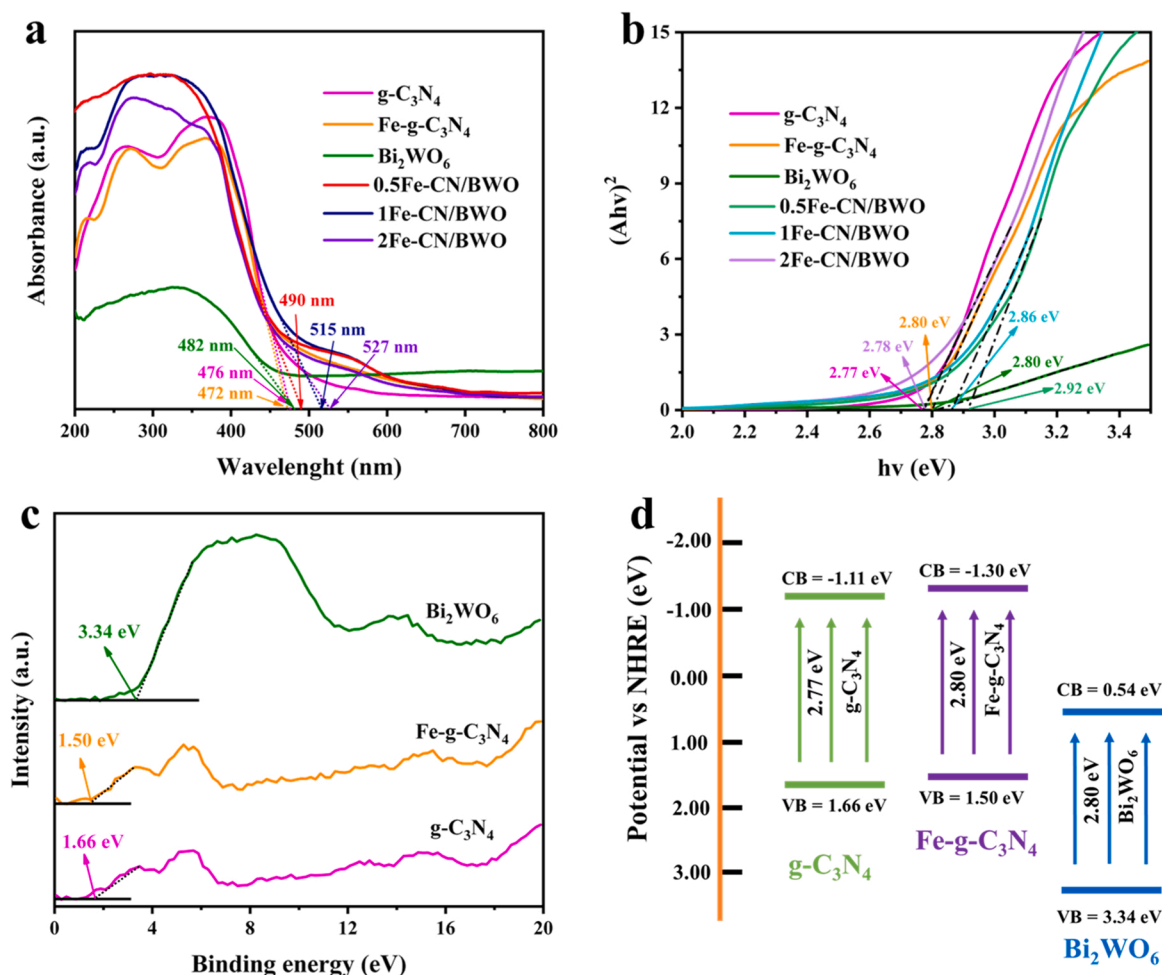


Fig. 2. (a) UV-vis DRS spectra of the prepared samples, (b) Tauc plots of the samples, (c) XPS VBs spectra of the prepared sample, and (d) electronic band structures of g-C₃N₄, Fe-g-C₃N₄ and Bi₂WO₆.

indicating that the photocatalytic performance of the sample is also enhanced.

Furthermore, as shown in Fig. 2c, the valence band edge potentials of g-C₃N₄, Fe-g-C₃N₄, and Bi₂WO₆ can be approximated to be 1.66 eV, 1.55 eV, and 3.34 eV respectively by referring to the XPS VB valence band spectra. There is a significant red-shift of optical absorption edges of Fe-g-C₃N₄, indicating that the coupling of g-C₃N₄ and Fe ions can significantly enhance the energy harvesting in the solar spectrum. Based on the results of bandgap and valence band, the conduction bands of g-C₃N₄, Fe-g-C₃N₄, and Bi₂WO₆ are calculated to be -1.11 eV, -1.30 eV, and 0.54 eV, respectively by the bandgap equation ($E_g = E_{VB} - E_{CB}$). Therefore, in Fig. 2d, the electronic energy band structures of Fe-g-C₃N₄ and Bi₂WO₆ can be designed in accordance with the results of bandgap, valence band, and conduction band, which can facilitate the analysis of the photocatalytic activity [50,51]. These results indicate that loading Fe onto g-C₃N₄ not only remarkably improves the optical absorption but also modulates the band structures.

3.3. Photo-Fenton catalytic activity

This study has explored the photo-Fenton activities of the series of composites as mentioned above for the degradation of TC under visible light irradiation. Fig. S4a-b is the comparison of the changes of TC removal efficiency and the reaction kinetic constants of Fe-CN/BWO composite under different concentrations of H₂O₂. Specifically, as the concentration of H₂O₂ is increased to 1 mM, the TC removal efficiency reached a maximum of 93.90% with a corresponding primary kinetic

constant of 0.02342 min⁻¹. However, when the H₂O₂ concentration is higher than 1 mM, there is no significant change in TC removal efficiency, which means that the increase of H₂O₂ concentration does not meaningfully improve the photo-Fenton catalytic degradation of TC to a certain extent. On the contrary, the TC removal efficiency decreases to 91.86% with a corresponding primary kinetic constant of 0.02076 min⁻¹ as the concentration of H₂O₂ is increased to 4 mM, suggesting that an increase in H₂O₂ concentration contributes to the photo-Fenton catalytic degradation of TC only when the H₂O₂ concentration is low. When the H₂O₂ concentration is high, the redundant H₂O₂ will function as a scavenger of hydroxyl radicals as well as a restrainer for iron-based catalysts reaction. Likewise, the trend in this study is with advanced oxidation techniques such as UV/H₂O₂ and the Fenton process. Yet it has been reported that in advanced oxidation techniques, too high a concentration of H₂O₂ will serve as a scavenger of free radicals. As the number of active radicals is reduced, the effectiveness of catalytic degradation of TC will be weakened too [52,53]. Therefore, the optimum H₂O₂ concentration required for the Fe-CN/BWO photo-Fenton degradation of a 10 mg/L TC solution should be as 1 mM to avoid additional treatment costs.

Meanwhile, the reactivity of the Fe-CN/BWO catalyst to activate the oxidation of TC by various oxidants like, peroxydisulfate (PDS), peroxydisulfate (PDS), hydrogen peroxide (H₂O₂), and potassium permanganate (KMnO₄) has been investigated in this study [54–56]. Fig. 3a shows that the degradation efficiency of TC is only 75.29%, 55.84%, 24.75% and 14% in the pure solutions systems of PMS, PDS, H₂O₂, and KMnO₄ respectively, while the degradation of TC can be effectively

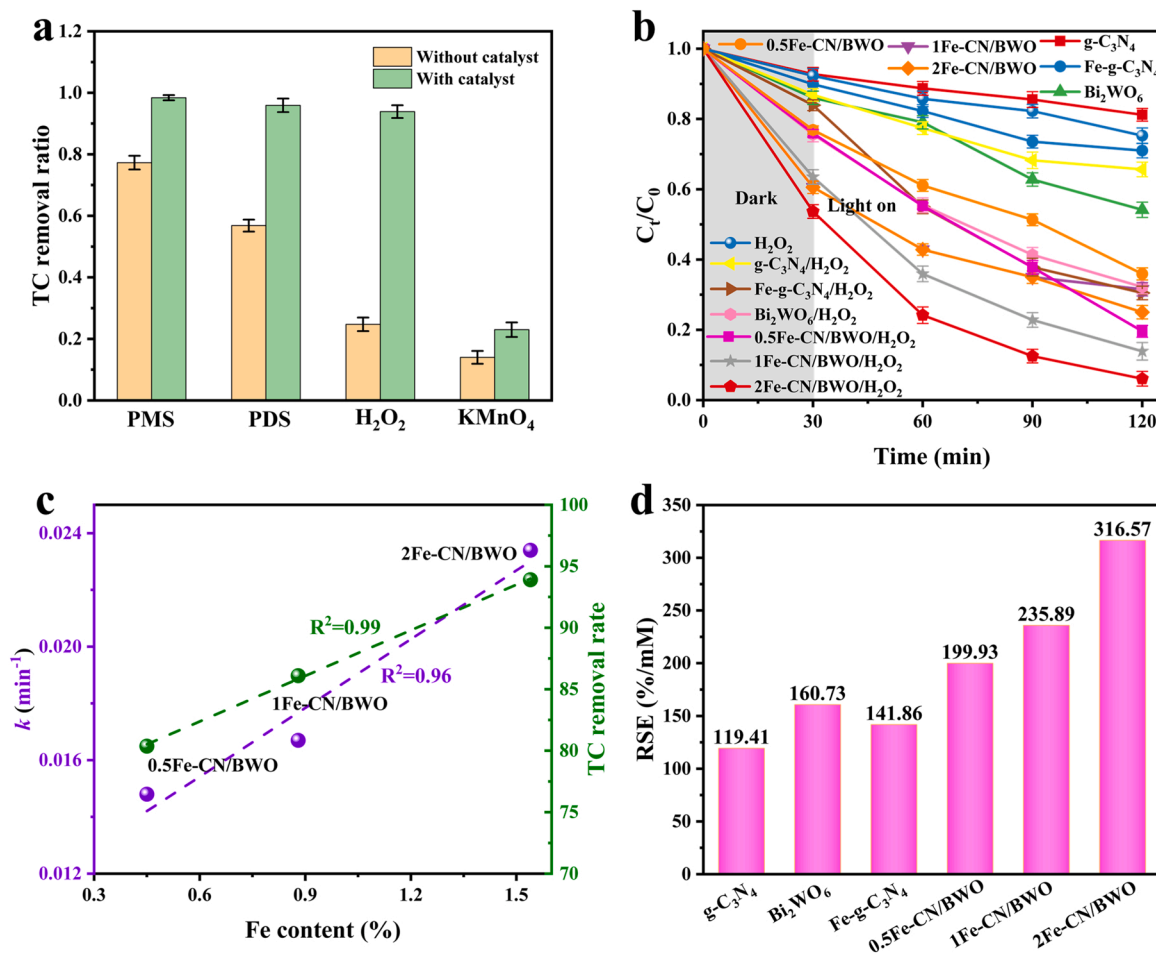


Fig. 3. (a) Removal ratio of TC in different oxidation systems by 120 min treatment time, (b) Degradation of TC by different composites, (c) The pseudo first-order kinetic constant of TC removal by Fe-CN/BWO catalyst, and the correlation between TC removal efficiency and different Fe content, and (d) Consumption of H₂O₂ in the different system. Reaction conditions: TC = 10 mg/L, [H₂O₂]₀ = 1 mM, [catalyst]₀ = 0.4 g/L, initial pollution pH = 6.5.

enhanced by the addition of a catalyst. Specifically, the Fe-CN/BWO/PMS, Fe-CN/BWO/PDS, Fe-CN/BWO/H₂O₂, and Fe-CN/BWO/KMnO₄ systems can achieve 98.42%, 95.93%, 93.90%, and 24% removal rate of TC respectively under the visible light irradiation within 120 min. However, the oxidative degradation of TC using PMS and PDS can lead to the secondary pollution of water bodies in that PMS and PDS will produce harmful SO₄²⁻ during the oxidation process. Therefore, this paper uses Fe-CN/BWO catalyst to activate H₂O₂ photo-Fenton to degrade TC in water.

Figs. 3b and S5 displays the effect of different Fe-doped contents and different percentages of Fe-CN and Bi₂WO₆ on the photo-Fenton degradation of TC. The pseudo-first-order and pseudo-second-order models have been used to investigate the kinetics of photo-Fenton degradation TC:

$$-\ln\left(\frac{C_t}{C_0}\right) = k_1 t \quad (2)$$

$$\frac{1}{C_t} - \frac{1}{C_0} = k_2 t \quad (3)$$

where C₀ and C_t are the concentrations of TC at 0 min and t min which refer to the photo-Fenton reaction time, while k₁ and k₂ are the proposed primary and secondary kinetic apparent rate constants. The apparent rate constants for the two kinetic models are shown in Table S2, and through the correlation coefficient (R²) it can be seen that the pseudo primary kinetic model is more consistent with the photocatalytic degradation of TC. Figs. 3b and S5 depicts the effect of different

composites on the photo-Fenton catalytic degradation of TC, showing that the H₂O₂, g-C₃N₄, Fe-g-C₃N₄, Bi₂WO₆, and Fe-CN/BWO photocatalytic degradation efficiency of TC is 24.75%, 18.79%, 28.98%, 45.85%, and 75.42%, respectively and the corresponding reaction rates are 0.00128, 0.00147, 0.00273, 0.00540 and 0.00969 min⁻¹. A remarkable improvement of TC degradation is observed with the addition of 1 mM H₂O₂ loading. Under such conditions, the degradation efficiency of 0.5Fe-CN/BWO, 1Fe-CN/BWO and 2Fe-CN/BWO is further increased to 80.37%, 86.10% and 93.90%, and the corresponding reaction rates turn to 0.0148, 0.01670 and 0.02342 min⁻¹, respectively. Compared with pure g-C₃N₄, Fe-g-C₃N₄, and Bi₂WO₆, all Fe-CN/BWO composites exhibit significantly higher photocatalytic activity and rate because of the formation of the Z-scheme heterojunction. Among the tested materials, 2-Fe-CN/BWO composite is identified as the most effective and selective catalyst, which achieves the highest degradation efficiency and rate constant, as 93.93% and 0.02342 min⁻¹, respectively. This occurrence reveals that doped Fe could greatly improve the catalytic performance of g-C₃N₄, probably due to the development of Fe-N₄ active sites in g-C₃N₄ [57]. With the successful doping of Fe-CN with Bi₂WO₆, the catalytic performance is maximized. The reason is probably that the constitution of a Z-scheme photocatalyst minimizes the compounding of photogenerated e⁻-h⁺ pairs to improve its catalytic performance, thus, by accelerating the transformation of Fe³⁺ to Fe²⁺ redox cycle in the Fe-CN/BWO composites and promoting the Fenton reaction with H₂O₂. It demonstrates that the photo-Fenton catalyst technology can perfectly combine photocatalysis with Fenton technology as excellent remediation of polluted water.

In order to study the relationship between Fe doping content and catalytic degradation of TC, the content of Fe in the catalyst was measured by ICP technology. The results show that the content of Fe in 0.5Fe-CN/BWO, 1Fe-CN/BWO and 2Fe-CN/BWO was 0.45 wt%, 0.88 wt% and 1.54 wt%, respectively. Through data fitting, the content of Fe in the catalyst is linearly and positively correlated with the reaction rate of TC ($R^2 = 0.96$) and the degradation rate ($R^2 = 0.99$) (Fig. 3c). Therefore, the more Fe in Fe-CN/BWO catalyst, the more Fe-N₄ bonds can be formed, so the catalytic performance is significantly improved.

In Fig. S6, the removal effectiveness of TC by Fe-CN/BWO composites in the presence of both H₂O₂ and xenon irradiation light increases significantly within 120 min to 93.90% in the photo-Fenton system. This is higher than the removal efficiency under only the photocatalysis (74.97%) or the Fenton reaction (64.93%), indicating that light could greatly enhance electron transfer and facilitate Fenton-like reactions due to the synergistic effect between photocatalysis and non-homogeneous Fenton-like reactions. In this study, the synergistic effects of photocatalysis (k_p) and heterogeneous Fenton-like (k_F) degradation rate have been determined based on their synergistic effects, as shown in Eq. (4).

$$\text{Synergy index} = \frac{k_{PF}}{k_p + k_F} \quad (4)$$

Where k_{PF} is the photo-Fenton degradation rate (k value), and the calculated results are shown in Table S3. According to this table, the synergistic index of the Fe-CN/BWO composite is calculated to be 1.615 (>1), a signal of a significant synergistic effect between the photocatalytic and non-homogeneous Fenton reactions.

In order to investigate the electron transfer pattern in the Fe-CN/BWO/H₂O₂ system, the utilization of H₂O₂ have been tested for different systems. The utilization efficiency of oxidant (H₂O₂) is expressed by reaction stoichiometric efficiency (RSE) (defined as the ratio of the percentage of degraded organic pollutants to oxidant consumption, Eq. (5)) (Fig. 3d). The higher the RSE value, the higher the utilization of H₂O₂. As RSE (316.57) of the 2Fe-CN/BWO/H₂O₂ system is higher than that of the g-C₃N₄/H₂O₂ System (119.41), Fe-g-C₃N₄/H₂O₂ System (141.86), Bi₂WO₆/H₂O₂ System (160.74), and 1Fe-CN/BWO/H₂O₂ System (235.89) (Table S4), it implies that the 2Fe-CN/BWO/H₂O₂ system can utilize H₂O₂ to the maximum.

$$\text{RSE} = \frac{\text{the percentage of oxidized TC}}{\text{consumption H}_2\text{O}_2} \quad (5)$$

The pH of the solution is frequently considered to be one of the important parameters for the oxidative degradation of TC. The degradation of TC by the Fe-CN/BWO/H₂O₂ in the photo-Fenton system have been investigated at different initial pH values (seven pH levels) in this study. As shown in Fig. S7, the degradation efficiency of TC at pH= 3, 4, and 10 reaches 97.10%, 96.32%, and 95.53% respectively within 120 min in the photo-Fenton system. The figure also shows that TC can be effectively removed in a wide pH range of 5–8 with the corresponding removal efficiency over 80%, which means that Fe-CN/BWO/H₂O₂ can overcome the disadvantage that normal Fenton and Fenton-like systems are only effective under acidic conditions. According to previous researches, the H₂O₂ process is more effective for the degradation of TC in weakly alkaline media than in acidic and neutral media [53]. However, the coupled Fe-CN/BWO Z-scheme photocatalysis proposed in the present study can extend its pH adaptability, and the degradation efficiency of the Fe-CN/BWO in the photo-Fenton system is over 85% at the pH range from 4 to 10. When the initial solution pH is highly alkaline (pH=13), the degradation efficiency of TC is reduced to a certain extent (only 74.52% after 120 min). It might be because H₂O₂ is easily decomposed to O₂ and H₂O in a strong alkaline environment, which will reduce the production of reactive oxygen species (ROS).

3.4. DFT theoretical calculation

To investigate the possible mechanisms affecting the photo-Fenton degradation of TC, DFT calculations have been applied to explore the interaction between the H₂O₂ molecule and the Fe doping sites. As shown in Fig. S8a-d, isolated Fe tends to occupy the quadruple ligand-doped configuration Fe-N₄ when Fe was doped into g-C₃N₄. The lattice parameters of g-C₃N₄ are $a=b=7.13 \text{ \AA}$, and $\gamma = 120^\circ$, while the doping of Fe turn the lattice parameters of Fe-g-C₃N₄ to $a=13.54 \text{ \AA}$, $b=13.79 \text{ \AA}$, and $\gamma = 120.2^\circ$ indicates that the doping of Fe causes g-C₃N₄ to fold, which provides more active sites for the photo-Fenton reaction. The density of states (DOS) patterns for g-C₃N₄ and Fe-g-C₃N₄ are displayed in Fig. S8e-f by theoretical calculations. It can be seen that the valence band maximum (VBM) of g-C₃N₄ is composed of N and C equivalents, whereas there is a predominance of N and a minority of C in the Conduction band minimum (CBM). But after the doping of Fe, Fe is synthesized in VBM and CBM [58]. In contrast to g-C₃N₄, the formation of Fe-N₄ induces a spin polarization of the material and also introduces a defect state in the original forbidden band, resulting in a broadening absorption of light and an enhancement of the lifetime of the photogenerated carriers. The model of Bi₂WO₆ with Fe-g-C₃N₄/Bi₂WO₆ is depicted in Fig. S9, from which it can be clearly seen that Fe-g-C₃N₄ forms a heterojunction with Bi₂WO₆, and then Fe will bond with O.

As shown in Fig. S10, the DFT calculated band gaps (E_g) for Bi₂WO₆ and g-C₃N₄ are 1.70 eV and 1.2 eV respectively, which is consistent with other theoretical studies but is less than the experimental value. It is possibly because the band gaps of the semiconductors are severely underestimated with the use of GGA calculations, but both are within the permissible range [59,60]. As can be seen from Fig. S10d, the doping of Fe induces a spin polarization in the monolayer g-C₃N₄, allowing the introduction of a defective energy band in the original forbidden band.

To further elaborate on the activation of H₂O₂ by Fe-N₄ sites, the adsorption energies of three different adsorption modes in which Fe-N₄ is adsorbed by H₂O₂ in Z-scheme catalyst Fe-CN/BWO have been calculated by DFT. In Fig. 4, Configuration I indicate that H₂O₂ adsorbed on Fe-CN/BWO will not dissociate, and the O of H₂O₂ is adsorbed directly on Fe, Configuration II indicates that H₂O₂ adsorbed on Fe-CN/BWO will dissociate into two •OH, one of which is adsorbed on Fe, and the other is adsorbed on the N site in Fe-N₄, Configuration III indicates that H₂O₂ adsorbed on Fe-CN/BWO undergoes dissociation into two •OH with one adsorbed on Fe and the other on the C site. The adsorption energies (E_{ads}) of H₂O₂ on the above three configurations are −1.19 eV, −2.34 eV, and 0.37 eV, respectively (Table S5). It suggests that H₂O₂ is stable for adsorption on Configuration I and Configuration II and unstable on Configuration III [16,61]. As adsorption energy of H₂O₂ on Configuration II (−2.34 eV) is lower than that of H₂O₂ on Configuration I. This indicates that the adsorption of H₂O₂ in the photo-Fenton reaction is more likely to occur in Configuration II adsorption, during which the two •OH adsorbed on the Fe site and the N site in Fe-N₄, respectively. Therefore, the investigational results and DFT calculations jointly show that the oxidation of TC has proceeded predominantly via Configuration II.

3.5. Analysis photo-Fenton system mechanism

The instantaneous photocurrent response is widely used to study photogenerated carrier production and interfacial transfer processes, for the instantaneous photocurrent value can directly reflect the separation efficiency and mobility of photogenerated carriers. Fig. S11a gives the outline of the photocurrent characteristics of the differently samples prepared in this study, illustrating that a uniform photocurrent density exists in all samples. With the increase of Fe content, the photocurrent intensity of the composite Fe-CN/BWO increases gradually. The 2Fe-CN/BWO composite exhibits the highest photocurrent density because the Z-scheme heterojunction formed between 2Fe-CN/BWO is more favorable for charge separation and transfer. It will lead to a longer

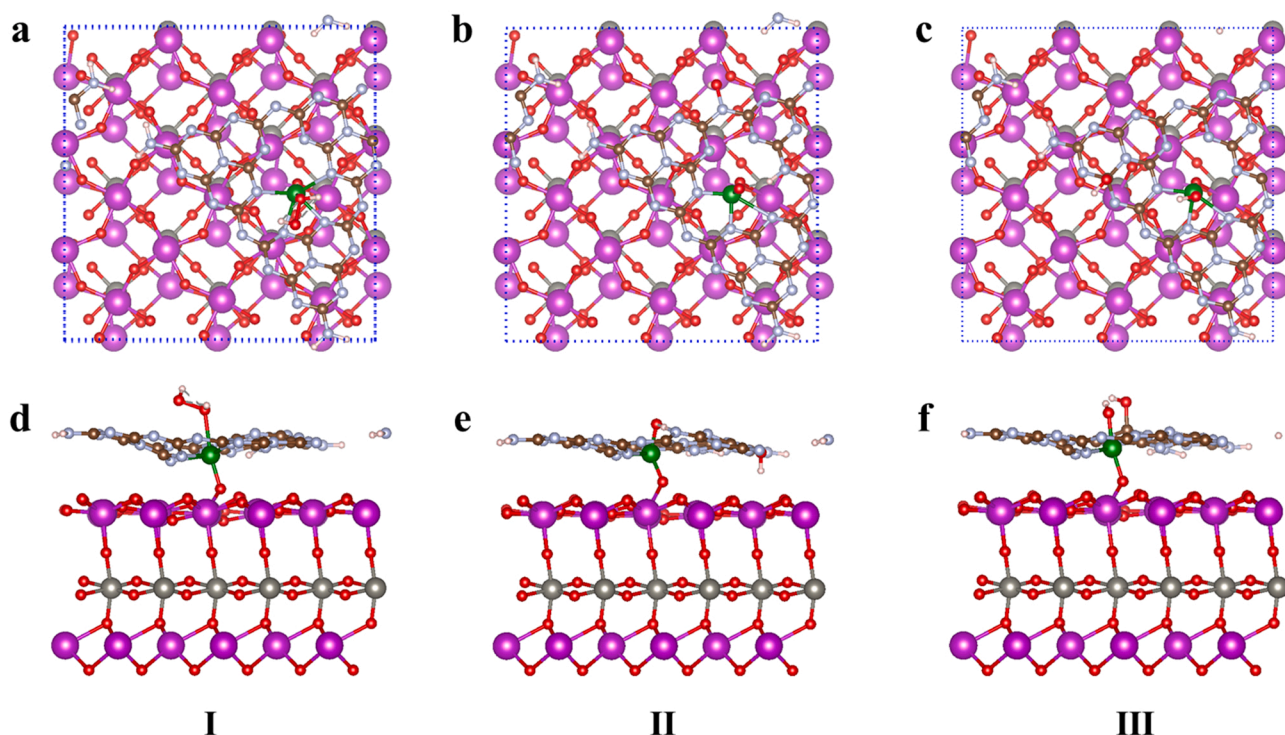


Fig. 4. H_2O_2 adsorbed on the superficial of the Z-scheme heterojunction (a) Configuration I, (b) Configuration II and (c) Configuration III top view, H_2O_2 adsorbed on the superficial of the Z scheme heterojunction (d) Configuration I, (e) Configuration II and (f) Configuration III side view.

lifetime of photogenerated carriers and then allow more electrons to participate in photodecomposition reactions, which is also consistent with the photocatalytic activity. In addition, electrochemical impedance spectroscopy (EIS) studies have been carried out to further demonstrate the photo-induced charge separation and migration efficiency of the prepared photocatalysts. The arc radius on the EIS spectrum reflects the resistance to delamination at the solid interface and the resistance to surface charge transfer, with a smaller radius indicating a more pronounced separation of photogenerated electrons and holes [49]. As shown in Fig. S11b, With the increase of Fe content in Fe-CN/BWO composites, the semicircular arc radius of EIS decreases gradually and 2Fe-CN/BWO has the smallest radius circle, indicating that the construction of heterojunctions can effectively reduce the resistance to the charge transfer and make it easier to involve more electrons and holes in the photo-Fenton reaction, corresponds with the results of photo-Fenton activity. From Fig. S11c, it can be observed that the intensity of 2Fe-CN/BWO, 1Fe-CN/BWO, and 0.5Fe-CN/BWO are much less than that of other samples, implying that the Z-scheme heterojunction can significantly inhibit the compounding of photogenerated electron holes so as to enhance the photo-Fenton degradation efficiency.

In order to further elucidate the mechanism for photo-Fenton catalytic degradation of TC by the Fe-CN/BWO/ H_2O_2 system, the capture experiments (Figs. 5a and S12) and ESR (Fig. 5b-d) characterization have been conducted to detect the main active species in the photo-Fenton process. In this study, EDTA-2Na, TBA, Hexachloroethane, and FFA are used as scavengers of h^+ , $\bullet\text{OH}$, $\bullet\text{O}_2^-$, and $^1\text{O}_2$, respectively. Fig. 5a provides a vivid description of the degradation efficiency of the Fe-CN/BWO/ H_2O_2 photo-Fenton system with the addition of EDTA-2Na, TBA, Hexachloroethane, and FFA separately [46,62–64]. When h^+ , $\bullet\text{OH}$ and $\bullet\text{O}_2^-$ are scavenged, the degradation efficiency of TC decreases from 93.90% to 81.95%, 82.72%, and 76.19%, implying that the three kinds of active species are involved in the TC degradation process with $\bullet\text{O}_2^-$ as the main ROS for TC photodegradation. This also suggests that these free radicals play an important role in the photo-Fenton degradation of TC. To further confirm the presence of ROS in the photo-Fenton process, ESR studies have been carried out with DMPO as

the trapping agent. In the dark, the Fe-CN/BWO composites did not produce DMPO- $\bullet\text{O}_2^-$ and DMPO- $\bullet\text{OH}$ signals, yet both of them appeared in the Fe-CN/BWO/ H_2O_2 system with the addition of H_2O_2 . It suggests that the addition of H_2O_2 contributes to the production of $\bullet\text{O}_2^-$ and $\bullet\text{OH}$ reactive oxygen species in the Fe-CN/BWO composites. Judging by the rapid increase of DMPO- $\bullet\text{O}_2^-$ and DMPO- $\bullet\text{OH}$ signals under visible light irradiation, more $\bullet\text{O}_2^-$ and $\bullet\text{OH}$ radicals can be generated under visible light. In addition, when the test conditions are illuminated without H_2O_2 , the signals of $\bullet\text{O}_2^-$ and $\bullet\text{OH}$ are significantly stronger than those in darkness, but slightly weaker than those in light Fenton reaction. This indicates that there is a synergistic effect between H_2O_2 and photocatalysis, which is consistent with the previous study.

Next, FFA has been chosen as a scavenger of $^1\text{O}_2$ to explore the presence of non-radical reactive oxygen species in the Fe-CN/BWO/ H_2O_2 system which proves that the degradation of TC is significantly inhibited to 69.32% by the addition of FFA. Because dissolved oxygen in water can promote the formation of $^1\text{O}_2$, $^1\text{O}_2$ capture experiments have been conducted in an N_2 atmosphere. The results show that the inhibitory effect of FFA on TC degradation is reduced to 53.27% under anoxic conditions (Fig. 5a). To further investigate the formation of $^1\text{O}_2$ in the Fe-CN/BWO/ H_2O_2 system, ESR experiments have been carried out using 2,2,6,6-tetramethylpiperidine (TEMP) as a spin trapping agent. As depicted in Fig. 5d, the strong 1:1:1 triplet state signal can be observed in Fe-CN/BWO/ H_2O_2 , further confirming the presence of $^1\text{O}_2$ in the Fe-CN/BWO/ H_2O_2 system.

In order to determine that Fe-CN/BWO photocatalyst is a Z-scheme heterojunction, the quenching experiment of Fe-CN/BWO photocatalytic degradation of TC was carried out. In Fig. S13, when h^+ , $\bullet\text{OH}$, $\bullet\text{O}_2^-$, $^1\text{O}_2$, and $^1\text{O}_2$ (in N_2 atmosphere) are scavenged, the degradation efficiency of TC decreases from 74.97% to 54.32%, 56.03%, 59.00%, 51.94%, and 43.13%, implying that the four kinds of active species are involved in the TC degradation process. In order to further confirm the existence of active substances in the photocatalytic process, ESR was studied using DMPO and TEMP as capture agents. As shown in Fig. S13c-e, the characteristic peaks of $\bullet\text{OH}$, $\bullet\text{O}_2^-$ and $^1\text{O}_2$ are not observed in the dark environment, indicating that the photocatalyst Fe-CN/BWO will

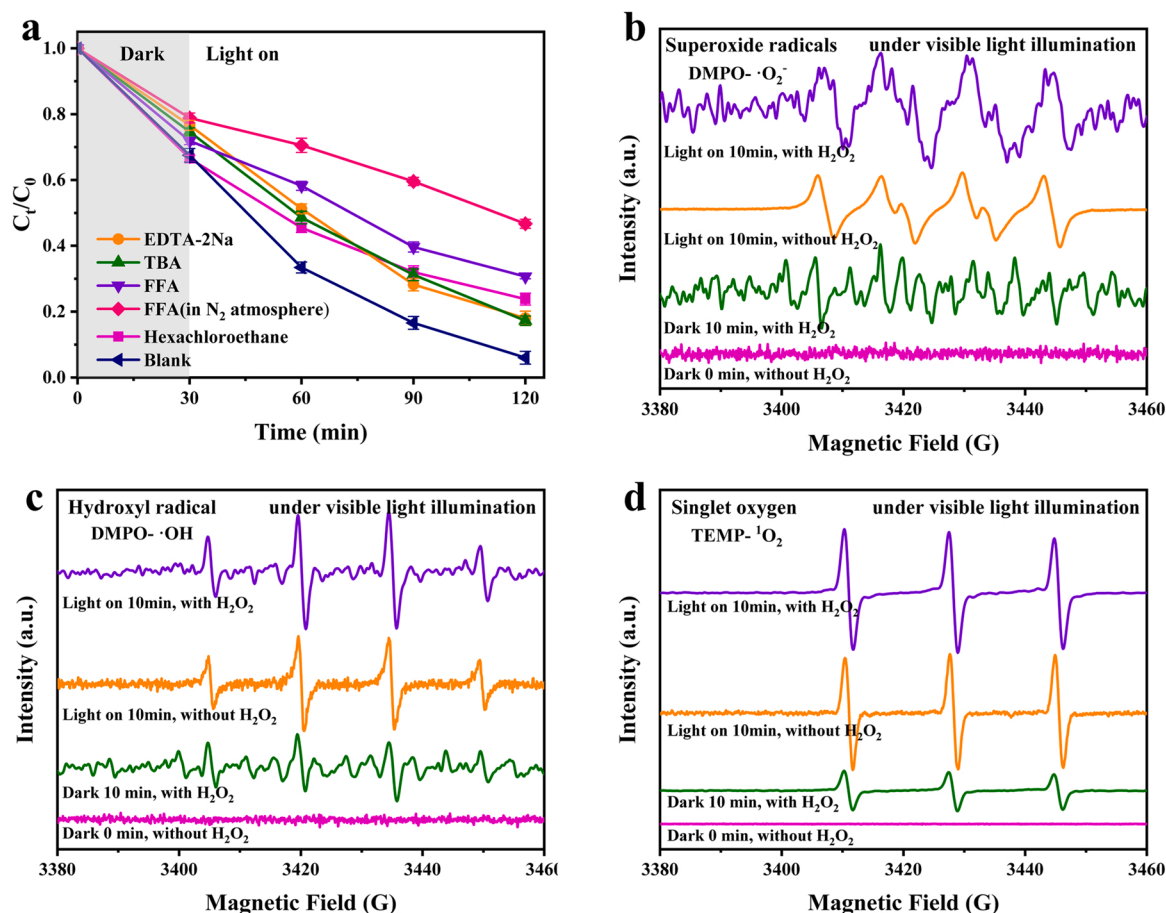


Fig. 5. (a) Effect of different scavengers on TC degradation in the Fe-CN/BWO/ H_2O_2 photo-Fenton system. ESR spectra of radical adducts trapped by DMPO: (b) superoxide radical ($\bullet O_2^-$) for Fe-CN/BWO composite and (c) hydroxyl radical ($\bullet OH$) in Fe-CN/BWO composite in the dark and under visible light irradiation, and (d) TEMP-trapped ESR spectra of 1O_2 . Reaction conditions: TC = 10 mg/L, catalyst dosage = 0.4 g/L, H_2O_2 concentration = 1 mM, initial pH = 6.5.

not produce $\bullet OH$, $\bullet O_2^-$ and 1O_2 active substances in the dark. Under illumination, the characteristic peaks of $\bullet OH$, $\bullet O_2^-$ and 1O_2 can be clearly seen in the ESR spectrum, indicating that the photocatalyst Fe-CN/BWO will produce $\bullet OH$, $\bullet O_2^-$ and 1O_2 active substances to degrade TC under illumination.

Based on UV-Vis DRS and XPS-VB data, the conduction band potentials of Fe-g-C₃N₄ and Bi₂WO₆ are -1.30 eV and 0.54 eV respectively, and the valence band potentials are 1.50 eV and 3.34 eV respectively. If the e^- of CB of Fe-g-C₃N₄ are transferred to CB of Bi₂WO₆, the h^+ of VB of Bi₂WO₆ are transferred to VB of Fe-g-C₃N₄ (Traditional heterojunction). The potential of CB (0.54 eV) of Bi₂WO₆ is not high enough to lead e^- to reduce O_2 to $\bullet O_2^-$ (-0.33 eV), and the potential of VB (1.50 eV) of Fe-g-C₃N₄ is much lower than the standard oxidation potential of $\bullet OH/H_2O$ (1.99 eV) and $\bullet OH/OH^-$ (2.68 eV), caused that h^+ unable to oxidize H_2O and OH^- to $\bullet OH$ [65–67]. This is inconsistent with the results of capture experiment and ESR. Therefore, when the e^- of the CB of Bi₂WO₆ are transferred to the VB of Fe-g-C₃N₄ (Z-scheme heterojunction), the CB (-1.30 eV) of Fe-g-C₃N₄ is sufficient to reduce O_2 to $\bullet O_2^-$, and the VB (3.34 eV) of Bi₂WO₆ is sufficient to oxidize H_2O and OH^- to $\bullet OH$. In this Z-scheme mechanism, the lower recombination rate of photogenerated electron-hole pairs and the longer lifetime of photogenerated carriers lead to the excellent photocatalytic degradation performance of Z-scheme photocatalyst Fe-CN/BWO.

Intending to further determine the formation of $\bullet OH$, $\bullet O_2^-$ and 1O_2 reactive oxygen species, XPS spectroscopy has been applied to characterize the surface composition and Z-scheme heterojunction structure of the composites. Fig. 6a shows that the presence of W, Bi, C, N, O, and Fe elements can be found in the full XPS spectra of the different composites

was observed, representing the successful synthesis of the composites. In Fig. 6b, the Fe 2p peaks at 710.39 eV and 723.88 eV correspond to the 2p_{3/2} and 2p_{1/2} orbitals of Fe²⁺ respectively, the peaks at 712.85 eV and 727.26 eV correspond to the 2p_{3/2} and 2p_{1/2} orbitals of Fe³⁺ respectively, while the peaks at 717.95 eV and 732.45 eV are associated with the satellite peaks of Fe²⁺ and Fe³⁺. It manifests that Fe is present in Fe-CN/BWO/ H_2O_2 in the form of Fe²⁺ and Fe³⁺ [68–71]. Besides, the percentages of Fe²⁺ and Fe³⁺ in the 2Fe-CN/BWO Z-scheme catalysts are 40.62% and 35.09%, indicating that the photo-Fenton system is dominated by Fe²⁺, which is consistent with the previous DFT calculations and further verifies the effect of Fe-N₄ sites on the degradation of TC. In addition, in order to clarify the important role of Fe-N₄ site in the degradation of TC, NaSCN and oxalate were added to the reaction system to form metal complexes and block the strong quenching catalytic reaction of Fe site [40]. Fig. S14 showed that the degradation of TC is significantly inhibited with the increase of the concentration of NaSCN and oxalate, indicating that the Fe-N₄ site plays an important role in the degradation of TC.

The high-resolution XPS spectra of Bi 4f (Fig. 6d) of the samples can be attributed to Bi³⁺ (158.66 eV and 163.93 eV) and Bi^{(3+x)+} (159.90 eV and 165.21 eV), which are due to the presence of surface defects in the Fe-CN/BWO composites. The Bi^{(3+x)+}/Bi³⁺ ratio of 2Fe-CN/BWO with Bi-O-Bi-O defective clusters is higher than that of 1Fe-CN/BWO and 0.5 Fe-CN/BWO, and no Bi^{(3+x)+} has been detected in Bi₂WO₆. Since the Bi 4f of 2Fe-CN/BWO and 1Fe-CN/BWO were shifted to lower values compared with Bi₂WO₆, it means that the electron density increased because of Fe atoms in Fe-CN/BWO. Furthermore, the asymmetric oxygen signal (Fig. 6e) can be fitted to three peaks, which

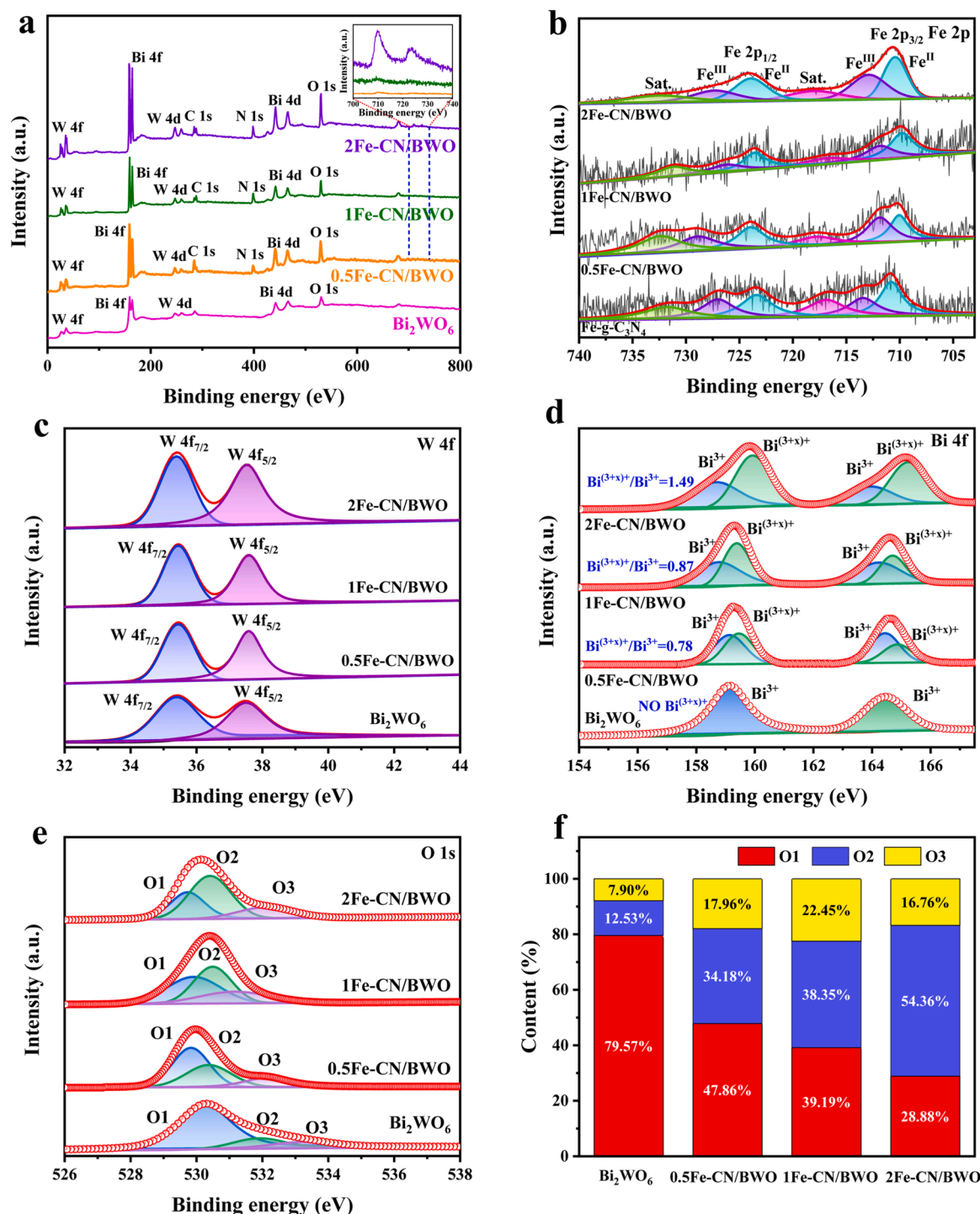


Fig. 6. XPS spectra of Bi_2WO_6 and Fe-CN/BWO: (a) Survey, (b) Fe 2p, (c) W 4f, (d) Bi 4f, (e) O 1s, and (f) the ratio of oxygen species in the sample.

are lattice oxygen (O1, 529.91 eV), surface vacancy oxygen (O2, 530.49 eV), and surface absorption oxygen (O3, 531.15 eV). As shown in Fig. 6f, 2Fe-CN/BWO has the highest surface vacancy oxygen content among all samples, which is conducive to oxygen mobility. The XPS data show that with the increase of Fe content, the ratio of $\text{Bi}^{(3+x)+}/\text{Bi}^{3+}$ and surface vacancy oxygen in Fe-CN/BWO composites gradually increases, and the performance of catalytic degradation of TC is also improved. The active species of $^1\text{O}_2$ in the Fe-CN/BWO/ H_2O_2 system may originate from Bi-O-Bi-O defective interactions. Compared to the Bi_2WO_6 sample, the O_2^- is converted to $^1\text{O}_2$ by the reaction $\text{Bi}^{(3+x)+} + \text{O}_2^- \rightarrow \text{Bi}^{3+} + ^1\text{O}_2$ due to the presence of $\text{Bi}^{(3+x)+}$ [72–74].

Based on these results, the mechanism of Fe-CN/BWO/ H_2O_2 photo-Fenton degradation of TC is proposed and illustrated in Fig. 7. In the dark, the $\bullet\text{OH}$ signal can still be detected in the Fe-CN/BWO/ H_2O_2 system, indicating that Fe^{2+} has reacted with H_2O_2 to form $\bullet\text{OH}$ (Eq. (6)). In addition, Fe^{2+} and Fe^{3+} have reacted with H_2O_2 respectively in the photo-Fenton system too (Eqs. (6) and (7)), thus achieving Fe cycling and extending its service life. The $\bullet\text{OH}$ signal is drastically enhanced in light due to the following reactions between the Z-scheme catalyst and H_2O_2 under visible light irradiation to produce $\bullet\text{OH}$ (Eqs. (8), (10)–(12)). The $\bullet\text{O}_2^-$ signal has also been observed in dark conditions, probably due to the decomposition of the peroxyhydroxyl group ($-\text{O}_2\text{H}$) to

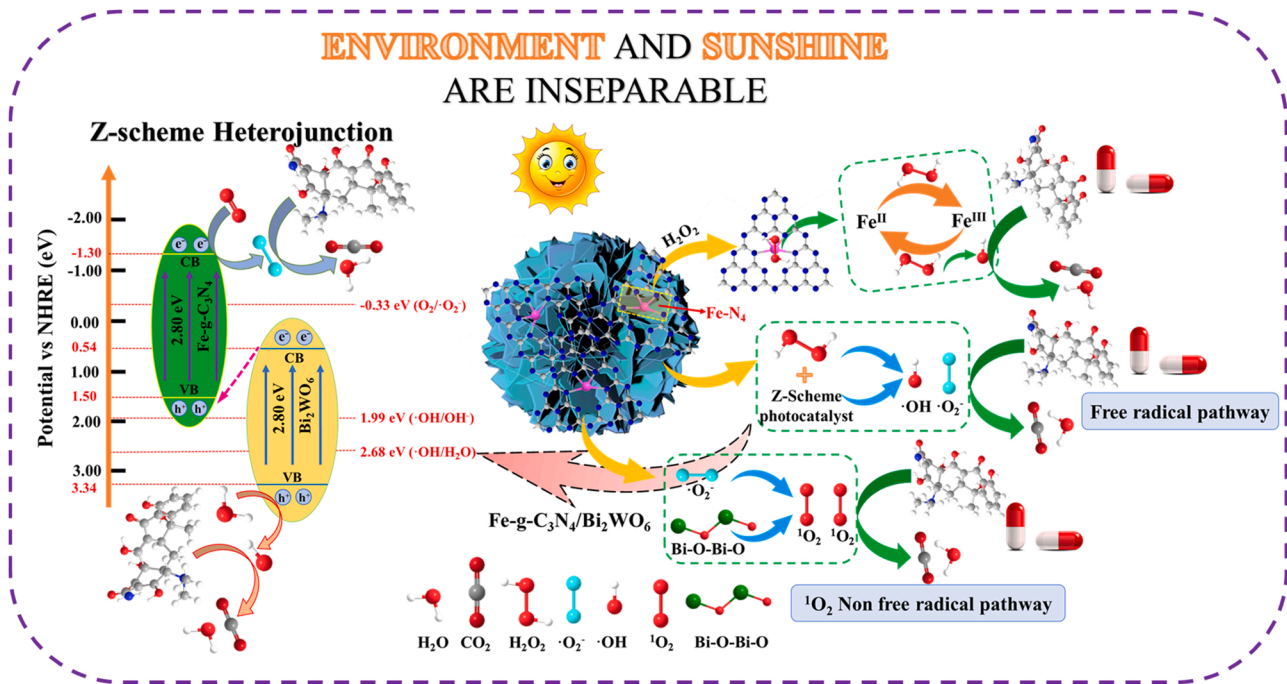
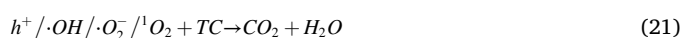


Fig. 7. Proposed photocatalytic mechanism over the Fe-CN/BWO/H₂O₂ photo-Fenton to degrade tetracycline.

produce $\bullet\text{O}_2^-$ (Eqs. (7), (13) and (14)). With the radiation of visible light, the Z-scheme catalyst Fe-CN/BWO absorbs light energy to produce h^+ and e^- , and O_2 is reduced by e^- to produce $\bullet\text{O}_2^-$ (Eq. (15)). The photo-generated electrons can be transported to the surface of Z-scheme catalyst Fe-CN/BWO to suppress the direct recombination of photo-generated electron-hole pairs so as to accelerate the transformation of Fe^{III} to Fe^{II} (Fe^{3+} to Fe^{2+} redox cycle) (Eqs. (9) and (16)) with strong reducing power in the presence of light, thus accelerating the inter-conversion between Fe^{3+} and Fe^{2+} to generate more $\bullet\text{OH}$ radicals in the presence of H_2O_2 . Furthermore, because the H_2O_2 can be decomposed by reaction with electrons, the rapid recombination of Z-scheme catalyst Fe-CN/BWO hole-electron pairs is further suppressed, which can create more holes for adsorption and strengthen the photo-Fenton catalytic capacity [75–78].

For the non-radical pathway, a signal for $^1\text{O}_2$ can be observed in dark conditions, which is generated probably through the conversion of $\bullet\text{O}_2^-$ radicals and $\bullet\text{OH}$ hydroxyl radicals (Eqs. (18)–(20)). Under visible light irradiation, Bi-O-Bi-O defective vacancies are created and then they are also converted to $^1\text{O}_2$. Meanwhile, under light the content of $\bullet\text{O}_2^-$ and $\bullet\text{OH}$ increases under light, consequently the $^1\text{O}_2$ signal is greatly enhanced under visible light (Eqs. (17)–(20)). The final pollutant is oxidized and degraded to CO_2 and H_2O by the action of active substances such as h^+ , $\bullet\text{OH}$, $\bullet\text{O}_2^-$, and $^1\text{O}_2$.



3.6. Proposed TC intermediates degradation pathways and toxicity estimation

The LC-MS analysis and DFT theoretical calculation have been conducted to reveal the pathways for the photo-Fenton catalytic degradation of TC. The double bonds, and phenolic and amine groups in the TC molecule have a high electron density and are susceptible to be attacked by reactive oxygen groups ($\bullet\text{OH}$, $\bullet\text{O}_2^-$ and $^1\text{O}_2$) during the degradation process, resulting in a range of intermediate products [79]. To figure out the pathways for the photo-Fenton degradation of TC, LC-MS has been used to test the intermediates of TC during the photo-Fenton reaction (Fig. S15). Based on this, three pathways for TC degradation are proposed in Fig. 8. Pathway I: The TC molecule is attacked by $\bullet\text{OH}$ and undergoes demethylation to produce product 1 ($m/z = 417$), which then is converted to product 2 ($m/z = 340$) by deamidation and hydroxylation. Subsequently, product 3 ($m/z = 326$) is further formed due to the loss of the methyl group. Afterwards, product 3 undergoes an open ring reaction to produce product 4 ($m/z = 171$), served as a substitute for the hydroxyl group by an aldehyde substitution reaction to produce product 5 ($m/z = 169$) [80]. Meanwhile, the amide group in product 2 ($m/z = 417$) might be attacked by $\bullet\text{OH}$ and $^1\text{O}_2$, and then may undergo a dehydration reaction to produce product 10 ($m/z = 362$). Subsequently,

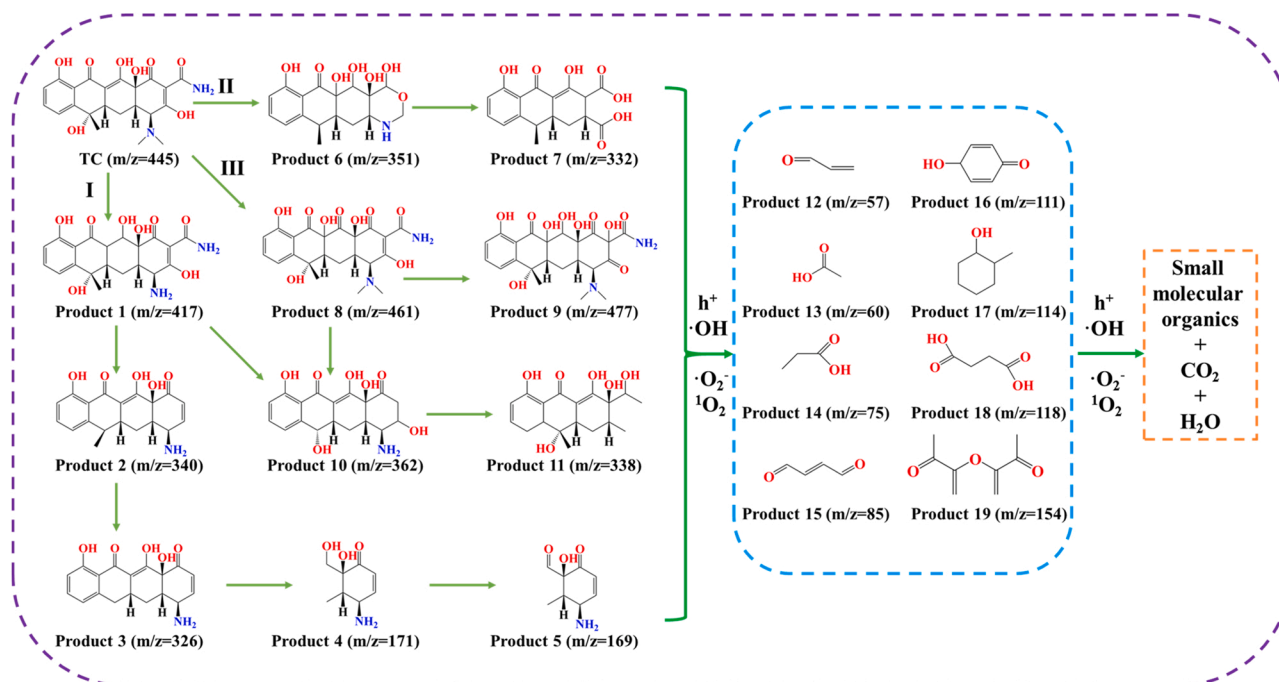


Fig. 8. Proposed degradation pathways of TC by the Fe-CN/BWO/H₂O₂ system.

with a further attack of $\bullet\text{OH}$, $\bullet\text{O}_2^-$, and $^1\text{O}_2$, product 10 will open the ring to produce product 11 ($m/z = 338$) [81]. Pathway II: The TC molecule undergoes the ring-opening, demethylation, and deamidation after being attacked by $\bullet\text{OH}$, $\bullet\text{O}_2^-$, and $^1\text{O}_2$ to produce product 6 ($m/z = 351$), and then the breakage of the ring of carbon atoms in product 6 will contribute to the formation of product 7 ($m/z = 332$) [82]. Pathway III: Product 8 ($m/z = 461$) is the hydroxylated product of the attack of $\bullet\text{OH}$, $\bullet\text{O}_2^-$, and $^1\text{O}_2$ on TC. Product 8 is then further attacked by $\bullet\text{OH}$, $\bullet\text{O}_2^-$, and $^1\text{O}_2$, leading to a multiple hydroxylation reaction to produce product 9 ($m/z = 477$) [9,83]. Ultimately, products 5, product 7, product 9 and product 11 all are degraded under the attack of h^+ , $\bullet\text{OH}$, $\bullet\text{O}_2^-$, and $^1\text{O}_2$ through ring-opening and loss of functional groups to produce some small organic molecules, which refer to product 12 ($m/z = 57$), product 13 ($m/z = 60$), product 14 ($m/z = 75$), product 15 ($m/z = 85$), product 16 ($m/z = 111$), product 17 ($m/z = 114$), product 18 ($m/z = 118$), and product 19 ($m/z = 154$). Finally, these small organic molecules are unceasingly decomposed into even smaller compounds until further completely mineralized to CO₂ and H₂O.

The toxicity of TC and its degradation intermediates have been analyzed by the Toxicity Estimation Software Tool (T.E.S.T.) [84,85]. The Fathead minnow LC₅₀, Daphnia magna LC₅₀, oral rat LD₅₀, and mutagenicity were obtained based on the quantitative structure-activity relationship (QSAR) method. For TC, the LC₅₀ values of Fathead minnow and Daphnia magna were 0.90 and 8.7 mg/L, which are rated as “Very toxic” and “toxic” respectively. For Fathead minnow (Fig. S16a), the LC₅₀ value for all intermediates is higher than TC, except for P1 (0.47 mg/L) and P7 (0.08 mg/L) which are lower than TC, greatly reducing the toxicity of the degradation intermediates. As indicated in Fig. S16b, Daphnia magna LC₅₀ had intermediates more than 8.7 mg/L except for P1 (3.19 mg/L), P2 (2.98 mg/L), P3 (3.35 mg/L), P7 (6.82 mg/L), P10 (6.92 mg/L) and P11 (5.43 mg/L). The oral LD₅₀ value for TC in rats shown in Fig. S16c is 1400.99 mg/kg and is assessed as “toxic”. The LD₅₀ values for P2 (1802.20 mg/kg), P3 (4278.17 mg/kg), P6 (1926.69 mg/kg), P11 (3155.76 mg/kg), P13 (1815.31 mg/kg), P17 (2050.64 mg/kg) and P18 (2499.04 mg/kg) are all higher in orally administered rats than in TC. In the aspect of mutagenicity toxicity (Fig. S16d), TC can be considered as a mutagenic organic pollutant. Fig. S16d illustrates that the Fe-CN/BWO/H₂O₂ photo-Fenton system

reduces the mutagenicity of most intermediates to “mutagenicity negative”. Therefore, it is supposed that TC is oxidized to be a less toxic product after the Z-scheme Fe-CN/BWO/H₂O₂ photo-Fenton reaction.

Fig. S17 presents a detailed description of the degradation of different pollutants. The Fe-CN/BWO catalyst shows good photo-Fenton degradation efficiency for all other antibiotics (CIP, OFX, and NOX), while the Z-scheme Fe-CN/BWO catalysts are also able to degrade BP-5R and MB rapidly by H₂O₂ activation of the photo-Fenton system. As shown in Fig. S18, the Fe-CN/BWO composites also displayed superior photo-Fenton degradation performance compared to g-C₃N₄, Fe-g-C₃N₄, and Bi₂WO₆.

The long-term operational stability and reusability of the Z-scheme Fe-CN/BWO catalyst are the keys to its practical use in daily life. Fig. S19a depicts the degradation effect of the Z-scheme catalyst recycled five times. The Fe leaching from Fe-CN/BWO during TC degradation has been measured using ICP-MS. After the first photo-Fenton degradation reaction of Fe-CN/BWO, the Fe leaching from the reaction solution reached 2.60 $\mu\text{g/L}$, which is much lower than the environmental standard (2 mg/L) [40,86]. After five cycles, the degradation rate of TC manifests a slight decline of 5% in the performance, which is a signal of its excellent reusability. Furthermore, the XRD and FTIR patterns (Fig. S19b-c) reveal that the used Fe-CN/BWO photocatalytic material shows no obvious changes in its chemical structures but remains well-matched with the fresh samples, which further verifies the stability of the structure during photodegradation. In order to further study the properties of the samples after photo-Fenton reaction, the stability of the samples was analyzed by XPS. As shown in Fig. S19d-f, there are characteristic peaks of W, O, N, C, Fe, and Bi in the full XPS spectrum of the samples before and after use, indicating that the chemical properties of the samples are stable. After photo-Fenton reaction, the contents of Fe and W did not decrease significantly, and the binding energy did not change significantly, which showed that the sample still had a relatively stable chemical structure after five photo-Fenton reactions.

3.7. Effect of co-existing anions and application of usage in the different water matrix

Natural water from different natural water bodies may contain many different organic matters and salts that may compete with TC to bind with reactive active sites of the catalyst. To explore the degradation of TC in actual water, the present study has investigated the degradation of TC in different water bodies (lake water, tap water, and deionized water) by Fe-CN/BWO/H₂O₂ photo-Fenton system. In Fig. S20a, a good degradation performance is achieved and the degradation efficiency of TC in lake water, tap water, and deionized water are 83.51%, 86.27%, and 93.90% respectively with the corresponding reaction constant as 0.0131, 0.0153, and 0.0234 min⁻¹. The test results of other water samples in both water matrices have shown some reduction in TC degradation, which might be caused by inorganic anions in the water or high concentrations of organic matter in the water covering the active sites of the catalyst or depleting the active groups. As a result, the interaction between TC and Fe-CN/BWO/H₂O₂ in the photo-Fenton system is affected, resulting in obvious inhibition of the catalytic performance of Fe-CN/BWO.

As shown in Fig. S20b, the humic acid (HA) in water inhibits the Fe-CN/BWO photo-Fenton degradation of TC and has an obvious negative effect. It may be attributed to the interaction between HA with the Fe-CN/BWO surface, which reduces the active site of Fe-CN/BWO towards TC. Alternatively, the HA forms a complex with TC via hydrogen and π - π bonds, which scavenges the reactive oxygen species and gives rise to the loss of activity on the Fe-CN/BWO surface [87].

The degradation of TC has been further investigated in the Fe-CN/BWO/H₂O₂ photo-Fenton system with the addition of some anions (Cl⁻, NO₃⁻, H₂PO₄⁻, and HCO₃⁻). The adverse degradation effect of Cl⁻ and NO₃⁻ on TC shown in Fig. S20c-d is negligible. In accordance with Fig. S20e, the degradation of TC is significantly inhibited with the addition of H₂PO₄⁻, which is probably because H₂PO₄⁻ may form complexes with the catalyst surface and then inhibit the degradation of TC [88]. Moreover, the addition of HCO₃⁻ anion can effectively promote the degradation of TC by Fe-CN/BWO/H₂O₂ photo-Fenton system (Fig. S20f). Since the \cdot OH is an important free radical for the degradation of TC, the addition of HCO₃⁻ can promote the increase of pH and then facilitate the production of \cdot OH despite that it will consume some of the \cdot OH too, thus eventually promoting the degradation of TC, according to the previous experiments on the effect of pH [89].

In order to figure out the differences in TC degradation rates and H₂O₂ utilization efficiency when H₂O₂ is injected into the TC solution in different ways. The H₂O₂ has been added into the reaction solution at one time and in batches to study the consumption of H₂O₂ in the system. Photo-Fenton degradation experiments have been carried out at TC concentrations of 10 mg/L under single (1 mM) and continuous H₂O₂ additions (2 \times 0.5 mM and 4 \times 0.25 mM) for comparison (Fig. S21a). After 120 min of reaction, more than 93.5% of TC are removed in the photo-Fenton system, yet the RSE of H₂O₂ is 0.316 in a single dose of 1 mM H₂O₂, while both the primary and secondary kinetic values of the reaction are the highest (Fig. S21b). To sum up, a single addition of H₂O₂ is more cost effective and cost-friendly in practical wastewater treatment, given the cost of H₂O₂, TC degradation efficiency as well as labor costs.

4. Conclusions

In this study, the Z-scheme Fe-CN/BWO catalyst has been successfully synthesized, which exhibits much better photo-Fenton catalytic performance for the degradation of TC in wastewater than other catalysts prepared as well in this study. Besides, Fe-CN/BWO can efficiently remove various other organics from wastewater. The excellent performance of Fe-CN/BWO is mainly ascribed to the facilitation effect of Fe-N₄ due to the spin polarization in the monolayer g-C₃N₄ induced by the doping of Fe as well as the Fe³⁺ to Fe²⁺ redox cycle regeneration during

the photo-Fenton reaction. Moreover, both synergistic effect and photogenerated charge carriers produced by Z-scheme photocatalyst can greatly accelerate the transfer rate of the charge carriers and effectively improve photocatalytic activity. According to the toxicity assessment obtained by the Toxicity estimation, a significant decrease of toxicity can be observed in the degradation intermediates compared to TC. Meanwhile, the ESR analysis proves that \bullet O₂⁻ and ¹O₂ are the primary contributors and play auxiliary roles in the degradation process. In addition, TC is oxidized by Z-scheme Fe-CN/BWO in the photo-Fenton reaction to a less toxic product via degradation intermediates analysis.

CRediT authorship contribution statement

Caihua Liu: Investigation, Methodology, Writing – original draft, Visualization. **Hongling Dai:** Resources, Writing – review & editing, Supervision. **Chaoqun Tan:** Resources, Writing – review & editing. **Qianyu Pan:** Resources, Writing – review & editing. **Fengping Hu:** Conceptualization, Writing – review & editing, Supervision. **Xiaoming Peng:** Conceptualization, Methodology, Writing – review & editing.

Declaration of Competing Interest

The authors declare that they have no known competing financial interests or personal relationships that could have appeared to influence the work reported in this paper.

Acknowledgments

This work was supported by the Natural Science Foundation of China (No. 51908213, 52160001, 51908214, 61872141), the Program of Major Disciplines, Academic and Technical Leaders of Jiangxi Province (20204BCJL23038), the Natural Science Foundation of Jiangxi Province (No. 20212ACB204003, 20201BBE51020) and State Key Laboratory of Pollution Control and Resource Reuse Foundation (No. PCRRF21028).

Appendix A. Supplementary information

Supplementary data associated with this article can be found in the online version at doi:10.1016/j.apcatb.2022.121326.

References

- [1] W. Shi, F. Guo, S. Yuan, In situ synthesis of Z-scheme Ag₃PO₄/CuBi₂O₄ photocatalysts and enhanced photocatalytic performance for the degradation of tetracycline under visible light irradiation, *Appl. Catal. B* 209 (2017) 720–728.
- [2] S. Murphy, C. Saurel, A. Morrissey, J. Tobin, M. Oelgemöller, K. Nolan, Photocatalytic activity of a porphyrin/TiO₂ composite in the degradation of pharmaceuticals, *Appl. Catal. B* 119–120 (2012) 156–165.
- [3] J. Guo, L. Wang, X. Wei, Z.A. Allothman, M.D. Albaqami, V. Malgras, Y. Yamauchi, Y. Kang, M. Wang, W. Guan, X. Xu, Direct Z-scheme CuInS₂/Bi₂MoO₆ heterostructure for enhanced photocatalytic degradation of tetracycline under visible light, *J. Hazard. Mater.* 415 (2021), 125591.
- [4] X. Xu, T. Yang, Q. Zhang, W. Xia, Z. Ding, K. Eid, A.M. Abdullah, M. Shahriar, A. Hossain, S. Zhang, J. Tang, L. Pan, Y. Yamauchi, Ultrahigh capacitive deionization performance by 3D interconnected MOF-derived nitrogen-doped carbon tubes, *Chem. Eng. J.* 390 (2020), 124493.
- [5] Y. Ben, C. Fu, M. Hu, L. Liu, M.H. Wong, C. Zheng, Human health risk assessment of antibiotic resistance associated with antibiotic residues in the environment: a review, *Environ. Res.* 169 (2019) 483–493.
- [6] F. Saadati, N. Keramati, M.M. Ghazi, Influence of parameters on the photocatalytic degradation of tetracycline in wastewater: a review, *Crit. Rev. Environ. Sci. Technol.* 46 (2016) 757–782.
- [7] F. Chen, Q. Yang, X. Li, G. Zeng, D. Wang, C. Niu, J. Zhao, H. An, T. Xie, Y. Deng, Hierarchical assembly of graphene-bridged Ag₃PO₄/Ag/BiVO₄ (040) Z-scheme photocatalyst: an efficient, sustainable and heterogeneous catalyst with enhanced visible-light photoactivity towards tetracycline degradation under visible light irradiation, *Appl. Catal. B* 200 (2017) 330–342.
- [8] B. Luo, D. Xu, D. Li, G. Wu, M. Wu, W. Shi, M. Chen, Fabrication of a Ag/Bi₃TaO₇ plasmonic photocatalyst with enhanced photocatalytic activity for degradation of tetracycline, *ACS Appl. Mater. Interfaces* 7 (2015) 17061–17069.
- [9] Y. Yang, Z. Zeng, C. Zhang, D. Huang, G. Zeng, R. Xiao, C. Lai, C. Zhou, H. Guo, W. Xue, M. Cheng, W. Wang, J. Wang, Construction of iodine vacancy-rich BiOI/Ag@AgI Z-scheme heterojunction photocatalysts for visible-light-driven

- tetracycline degradation: transformation pathways and mechanism insight, *Chem. Eng. J.* 349 (2018) 808–821.
- [10] D. Huang, X. Wang, C. Zhang, G. Zeng, Z. Peng, J. Zhou, M. Cheng, R. Wang, Z. Hu, X. Qin, Sorptive removal of ionizable antibiotic sulfamethazine from aqueous solution by graphene oxide-coated biochar nanocomposites: Influencing factors and mechanism, *Chemosphere* 186 (2017) 414–421.
 - [11] X. Peng, Z. Yang, F. Hu, C. Tan, Q. Pan, H. Dai, Mechanistic investigation of rapid catalytic degradation of tetracycline using $\text{CoFe}_2\text{O}_4/\text{MoS}_2$ by activation of peroxymonosulfate, *Sep. Purif. Technol.* 287 (2022), 120525.
 - [12] Z. Xie, Y. Peng, F. Wang, D. Chen, Q. Zhang, Y. Zeng, W. Lv, G. Liu, Construction of carbon dots modified $\text{MoO}_3/\text{g-C}_3\text{N}_4$ Z-scheme photocatalyst with enhanced visible-light photocatalytic activity for the degradation of tetracycline, *Appl. Catal. B* 229 (2018) 96–104.
 - [13] B. Wang, C. Bozal-Ginesta, R. Zhang, B. Zhou, H. Ma, L. Jiao, L. Xu, E. Liu, C. Wang, Z. Li, A supramolecular $\text{H}_2\text{SubPcB-OPhCOPh/TiO}_2$ Z-scheme hybrid assembled via dimeric concave-ligand π -interaction for visible photocatalytic oxidation of tetracycline, *Appl. Catal. B* 298 (2021), 120550.
 - [14] K. Li, Y. Zhong, S. Luo, W. Deng, Fabrication of powder and modular $\text{H}_3\text{PW}_{12}\text{O}_{40}/\text{Ag}_3\text{PO}_4$ composites: novel visible-light photocatalysts for ultra-fast degradation of organic pollutants in water, *Appl. Catal. B* 278 (2020), 119313.
 - [15] G. Matafonova, V. Batoev, Recent advances in application of UV light-emitting diodes for degrading organic pollutants in water through advanced oxidation processes: a review, *Water Res.* 132 (2018) 177–189.
 - [16] X. Peng, J. Wu, Z. Zhao, X. Wang, H. Dai, Y. Wei, G. Xu, F. Hu, Activation of peroxymonosulfate by single atom Co-N-C catalysts for high-efficient removal of chloroquine phosphate via non-radical pathways: Electron-transfer mechanism, *Chem. Eng. J.* 429 (2022), 132245.
 - [17] C. Wang, H. Wang, J. Na, Y. Yao, A. Azhar, X. Yan, J. Qi, Y. Yamauchi, J. Li, 0D–1D hybrid nanoarchitectonics: tailored design of FeCo@N-C yolk-shell nanoreactors with dual sites for excellent Fenton-like catalysis, *Chem. Sci.* 12 (2021) 15418–15422.
 - [18] K. Li, Y. Liang, H. Yang, S. An, H. Shi, C. Song, X. Guo, New insight into the mechanism of enhanced photo-Fenton reaction efficiency for Fe-doped semiconductors: a case study of $\text{Fe-g-C}_3\text{N}_4$, *Catal. Today* 371 (2021) 58–63.
 - [19] J. Wang, S. Wang, Removal of pharmaceuticals and personal care products (PPCPs) from wastewater: a review, *J. Environ. Manag.* 182 (2016) 620–640.
 - [20] C. Li, H. Wu, D. Zhu, T. Zhou, M. Yan, G. Chen, J. Sun, G. Dai, F. Ge, H. Dong, High-efficient charge separation driven directionally by pyridine rings grafted on carbon nitride edge for boosting photocatalytic hydrogen evolution, *Appl. Catal. B* 297 (2021), 120433.
 - [21] C. Li, D. Zhu, S. Cheng, Y. Zuo, Y. Wang, C. Ma, H. Dong, Recent research progress of bimetallic phosphides-based nanomaterials as cocatalyst for photocatalytic hydrogen evolution, *Chin. Chem. Lett.* (2021), <https://doi.org/10.1016/j.ccl.2021.07.057>.
 - [22] S. Yanan, X. Xing, Q. Yue, B. Gao, Y. Li, Nitrogen-doped carbon nanotubes encapsulating Fe/Zn nanoparticles as a persulfate activator for sulfamethoxazole degradation: role of encapsulated bimetallic nanoparticles and nonradical reaction, *Environ. Sci. Nano* 7 (2020) 1444–1453.
 - [23] J. Ma, K. Wang, C. Wang, X. Chen, W. Zhu, G. Zhu, W. Yao, Y. Zhu, Photocatalysis-self-Fenton system with high-fluent degradation and high mineralization ability, *Appl. Catal. B* 276 (2020), 119150.
 - [24] Z. Cao, Y. Jia, Q. Wang, H. Cheng, High-efficiency photo-Fenton $\text{Fe/g-C}_3\text{N}_4/\text{kaolinite}$ catalyst for tetracycline hydrochloride degradation, *Appl. Clay Sci.* 212 (2021), 106213.
 - [25] D. Huang, S. Chen, G. Zeng, X. Gong, C. Zhou, M. Cheng, W. Xue, X. Yan, J. Li, Artificial Z-scheme photocatalytic system: what have been done and where to go? *Coord. Chem. Rev.* 385 (2019) 44–80.
 - [26] W. Zhao, Y. Li, P. Zhao, L. Zhang, B. Dai, J. Xu, H. Huang, Y. He, D.Y.C. Leung, Novel Z-scheme $\text{Ag-C}_3\text{N}_4/\text{SnS}_2$ plasmonic heterojunction photocatalyst for degradation of tetracycline and H_2 production, *Chem. Eng. J.* 405 (2021), 126555.
 - [27] W. Chang, W. Xue, E. Liu, J. Fan, B. Zhao, Highly efficient H_2 production over NiCo_2O_4 decorated $\text{g-C}_3\text{N}_4$ by photocatalytic water reduction, *Chem. Eng. J.* 362 (2019) 392–401.
 - [28] C. Ouyang, X. Quan, C. Zhang, Y. Pan, X. Li, Z. Hong, M. Zhi, Direct Z-scheme $\text{ZnIn}_2\text{S}_4/\text{MoO}_3$ heterojunction for efficient photodegradation of tetracycline hydrochloride under visible light irradiation, *Chem. Eng. J.* 424 (2021), 130510.
 - [29] I. Vassalini, G. Ribaudo, A. Gianoncelli, M.F. Casula, I. Alessandri, Plasmonic hydrogels for capture, detection and removal of organic pollutants, *Environ. Sci. Nano* 7 (2020) 3888–3900.
 - [30] X. Wei, X. Wang, Y. Pu, A. Liu, C. Chen, W. Zou, Y. Zheng, J. Huang, Y. Zhang, Y. Yang, M. Naushad, B. Gao, L. Dong, Facile ball-milling synthesis of $\text{CeO}_2/\text{g-C}_3\text{N}_4$ Z-scheme heterojunction for synergistic adsorption and photodegradation of methylene blue: characteristics, kinetics, models, and mechanisms, *Chem. Eng. J.* 420 (2021), 127719.
 - [31] D. Huang, J. Li, G. Zeng, W. Xue, S. Chen, Z. Li, R. Deng, Y. Yang, M. Cheng, Facile construction of hierarchical flower-like Z-scheme $\text{AgBr/Bi}_2\text{WO}_6$ photocatalysts for effective removal of tetracycline: degradation pathways and mechanism, *Chem. Eng. J.* 375 (2019), 121991.
 - [32] X. Wang, M. He, Z. Nan, Effects of adsorption capacity and activity site on Fenton-like catalytic performance for Na and Fe co-doped $\text{g-C}_3\text{N}_4$, *Sep. Purif. Technol.* 256 (2021), 117765.
 - [33] X. Zeng, Y. Liu, Y. Kang, Q. Li, Y. Xia, Y. Zhu, H. Hou, M.H. Uddin, T. R. Gengenbach, D. Xia, C. Sun, D.T. McCarthy, A. Deletic, J. Yu, X. Zhang, Simultaneously tuning charge separation and oxygen reduction pathway on graphitic carbon nitride by polyethylenimine for boosted photocatalytic hydrogen peroxide production, *ACS Catal.* 10 (2020) 3697–3706.
 - [34] H. Cao, J. Wang, J.-H. Kim, Z. Guo, J. Xiao, J. Yang, J. Chang, Y. Shi, Y. Xie, Different roles of Fe atoms and nanoparticles on $\text{g-C}_3\text{N}_4$ in regulating the reductive activation of ozone under visible light, *Appl. Catal. B* 296 (2021), 120362.
 - [35] X. Wang, X. Chen, A. Thomas, X. Fu, M. Antonietti, Metal-containing carbon nitride compounds: a new functional organic-metal hybrid material, *Adv. Mater.* 21 (2009) 1609–1612.
 - [36] L. Yan, Y. Wang, H. Shen, Y. Zhang, J. Li, D. Wang, Photocatalytic activity of $\text{Bi}_2\text{WO}_6/\text{Bi}_2\text{S}_3$ heterojunctions: the facilitation of exposed facets of Bi_2WO_6 substrate, *Appl. Surf. Sci.* 393 (2017) 496–503.
 - [37] W. Xue, D. Huang, J. Li, G. Zeng, R. Deng, Y. Yang, S. Chen, Z. Li, X. Gong, B. Li, Assembly of AgI nanoparticles and ultrathin $\text{g-C}_3\text{N}_4$ nanosheets codecorated Bi_2WO_6 direct dual Z-scheme photocatalyst: an efficient, sustainable and heterogeneous catalyst with enhanced photocatalytic performance, *Chem. Eng. J.* 373 (2019) 1144–1157.
 - [38] J. Wang, L. Tang, G. Zeng, Y. Deng, Y. Liu, L. Wang, Y. Zhou, Z. Guo, J. Wang, C. Zhang, Atomic scale $\text{g-C}_3\text{N}_4/\text{Bi}_2\text{WO}_6$ 2D/2D heterojunction with enhanced photocatalytic degradation of ibuprofen under visible light irradiation, *Appl. Catal. B* 209 (2017) 285–294.
 - [39] B. Chong, L. Chen, W. Wang, D. Han, L. Wang, L. Feng, Q. Li, C. Li, Visible-light-driven Ag-decorated $\text{g-C}_3\text{N}_4/\text{Bi}_2\text{WO}_6$ Z-scheme composite for high photocatalytic activity, *Mater. Lett.* 204 (2017) 149–153.
 - [40] X. Peng, J. Wu, Z. Zhao, X. Wang, H. Dai, L. Xu, G. Xu, Y. Jian, F. Hu, Activation of peroxymonosulfate by single-atom $\text{Fe-g-C}_3\text{N}_4$ catalysts for high efficiency degradation of tetracycline via nonradical pathways: role of high-valent iron-oxo species and Fe-N_x sites, *Chem. Eng. J.* 427 (2022), 130803.
 - [41] D. Wang, H. Xu, P. Yang, X. Lu, J. Ma, R. Li, L. Xiao, J. Zhang, M. An, Fe-N_x and Co-N_x dual sites for boosting oxygen electroreduction in Zn-air batteries, *J. Mater. Chem. A* 9 (2021) 13678–13687.
 - [42] B. Zhang, X. Li, K. Akiyama, P.A. Bingham, S. Kubuki, Elucidating the mechanistic origin of a spin state-dependent $\text{FeN}_x\text{-C}$ catalyst toward organic contaminant oxidation via peroxymonosulfate activation, *Environ. Sci. Technol.* 56 (2022) 1321–1330.
 - [43] Y. Shang, X. Duan, S. Wang, Q. Yue, B. Gao, X. Xu, Carbon-based single atom catalyst: synthesis, characterization, DFT calculations, *Chin. Chem. Lett.* 33 (2021) 663–673.
 - [44] J. Hu, P. Zhang, W. An, L. Liu, Y. Liang, W. Cui, In-situ Fe-doped $\text{g-C}_3\text{N}_4$ heterogeneous catalyst via photocatalysis-Fenton reaction with enriched photocatalytic performance for removal of complex wastewater, *Appl. Catal. B* 245 (2019) 130–142.
 - [45] Z. Jiang, W. Wan, H. Li, S. Yuan, H. Zhao, P.K. Wong, A hierarchical Z-scheme $\alpha\text{-Fe}_2\text{O}_3/\text{g-C}_3\text{N}_4$ hybrid for enhanced photocatalytic CO_2 reduction, *Adv. Mater.* 30 (2018) 1706108.
 - [46] Z. Xie, Y. Peng, F. Wang, D. Chen, Q. Zhang, Y. Zeng, W. Lv, G. Liu, Construction of carbon dots modified $\text{MoO}_3/\text{g-C}_3\text{N}_4$ Z-scheme photocatalyst with enhanced visible-light photocatalytic activity for the degradation of tetracycline, *Appl. Catal. B* 229 (2018) 96–104.
 - [47] Y. Wang, W. Jiang, W. Luo, X. Chen, Y. Zhu, Ultrathin nanosheets $\text{g-C}_3\text{N}_4/\text{Bi}_2\text{WO}_6$ core-shell structure via low temperature reassembled strategy to promote photocatalytic activity, *Appl. Catal. B* 237 (2018) 633–640.
 - [48] Z. Lv, H. Zhou, H. Liu, B. Liu, M. Liang, H. Guo, Controlled assemble of oxygen vacant $\text{CeO}_2/\text{Bi}_2\text{WO}_6$ hollow magnetic microcapsule heterostructures for visible-light photocatalytic activity, *Chem. Eng. J.* 330 (2017) 1297–1305.
 - [49] K. Zhang, J. Wang, W. Jiang, W. Yao, H. Yang, Y. Zhu, Self-assembled perylene diimide based supramolecular heterojunction with Bi_2WO_6 for efficient visible-light-driven photocatalysis, *Appl. Catal. B* 232 (2018) 175–181.
 - [50] D. Zhu, Q. Zhou, Novel Bi_2WO_6 modified by N-doped graphitic carbon nitride photocatalyst for efficient photocatalytic degradation of phenol under visible light, *Appl. Catal. B* 268 (2020), 118426.
 - [51] Z. Jiang, X. Liang, H. Zheng, Y. Liu, Z. Wang, P. Wang, X. Zhang, X. Qin, Y. Dai, M.-H. Whangbo, B. Huang, Photocatalytic reduction of CO_2 to methanol by three-dimensional hollow structures of Bi_2WO_6 quantum dots, *Appl. Catal. B* 219 (2017) 209–215.
 - [52] L. Hou, L. Wang, S. Royer, H. Zhang, Ultrasound-assisted heterogeneous Fenton-like degradation of tetracycline over a magnetite catalyst, *J. Hazard. Mater.* 302 (2016) 458–467.
 - [53] Y.-Y. Chen, Y.-L. Ma, J. Yang, L.-Q. Wang, J.-M. Lv, C.-J. Ren, Aqueous tetracycline degradation by H_2O_2 alone: removal and transformation pathway, *Chem. Eng. J.* 307 (2017) 15–23.
 - [54] S. Yang, S. Xu, J. Tong, D. Ding, G. Wang, R. Chen, P. Jin, X.C. Wang, Overlooked role of nitrogen dopant in carbon catalysts for peroxymonosulfate activation: intrinsic defects or extrinsic defects? *Appl. Catal. B* 295 (2021), 120291.
 - [55] S. Cai, Q. Zhang, Z. Wang, S. Hua, D. Ding, T. Cai, R. Zhang, Pyrrolic N-rich biochar without exogenous nitrogen doping as a functional material for bisphenol A removal: performance and mechanism, *Appl. Catal. B* 291 (2021), 120093.
 - [56] Z. Wang, C. Du, S. Lei, D. Ding, R. Chen, S. Yang, T. Cai, Modulation of carbon induced persulfate activation by nitrogen dopants: recent advances and perspectives, *J. Mater. Chem. A* 9 (2021) 25796–25826.
 - [57] Q. Li, H. Xu, G. Zhou, F. Cheng, M. Wang, J. Zhang, Y. Wang, X. Huang, Q. Wang, Sulfite activation by Fe-doped $\text{g-C}_3\text{N}_4$ for metronidazole degradation, *Sep. Purif. Technol.* 272 (2021), 118928.
 - [58] D. Yang, X. Cai, J. Zhang, B. Ding, Y. Zhao, X. Gu, L. Mao, Y. Qiang, Preparation of 0D/2D $\text{ZnFe}_2\text{O}_4/\text{Fe-doped g-C}_3\text{N}_4$ hybrid photocatalysts for visible light N_2 fixation, *J. Alloy. Compd.* 869 (2021), 158809.
 - [59] M. Cao, L. Ni, Z. Wang, J. Liu, Y. Tian, Y. Zhang, X. Wei, T. Guo, J. Fan, L. Duan, DFT investigation on direct Z-scheme photocatalyst for overall water splitting: MoTe_2/BAs van der Waals heterostructure, *Appl. Surf. Sci.* 551 (2021), 149364.

- [60] H. Dong, Y. Zuo, N. Song, S. Hong, M. Xiao, D. Zhu, J. Sun, C. Gao, C. Li, Bimetallic synergistic regulating effect on electronic structure in cobalt/vanadium co-doped carbon nitride for boosting photocatalytic performance, *Appl. Catal. B* 287 (2021), 119954.
- [61] F. Yang, M. Wang, W. Liu, B. Yang, Y. Wang, J. Luo, Y. Tang, L. Hou, Y. Li, Z. Li, B. Zhang, W. Yang, Y. Li, Atomically dispersed Ni as the active site towards selective hydrogenation of nitroarenes, *Green Chem.* 21 (2019) 704–711.
- [62] Y. Tian, W. Li, C. Zhao, Y. Wang, B. Zhang, Q. Zhang, Fabrication of hollow mesoporous $\text{SiO}_2\text{-BiOCl@PANI@Pd}$ photocatalysts to improve the photocatalytic performance under visible light, *Appl. Catal. B* 213 (2017) 136–146.
- [63] F. Chen, Q. Yang, X. Li, G. Zeng, D. Wang, C. Niu, J. Zhao, H. An, T. Xie, Y. Deng, Hierarchical assembly of graphene-bridged $\text{Ag}_3\text{PO}_4/\text{Ag/BiVO}_4$ (040) Z-scheme photocatalyst: an efficient, sustainable and heterogeneous catalyst with enhanced visible-light photoactivity towards tetracycline degradation under visible light irradiation, *Appl. Catal. B* 200 (2017) 330–342.
- [64] J. Guo, L. Wang, X. Wei, Z.A. Allothman, M.D. Albaqami, V. Malgras, Y. Yamauchi, Y. Kang, M. Wang, W. Guan, X. Xu, Direct Z-scheme $\text{CuInS}_2/\text{Bi}_2\text{MoO}_6$ heterostructure for enhanced photocatalytic degradation of tetracycline under visible light, *J. Hazard. Mater.* 415 (2021), 125591.
- [65] M. Tang, Y. Ao, C. Wang, P. Wang, Rationally constructing of a novel dual Z-scheme composite photocatalyst with significantly enhanced performance for neonicotinoid degradation under visible light irradiation, *Appl. Catal. B* 270 (2020), 118918.
- [66] M. Tang, Y. Ao, C. Wang, P. Wang, Facile synthesis of dual Z-scheme $\text{g-C}_3\text{N}_4/\text{Ag}_3\text{PO}_4/\text{AgI}$ composite photocatalysts with enhanced performance for the degradation of a typical neonicotinoid pesticide, *Appl. Catal. B* 268 (2020), 118395.
- [67] X. Peng, C. Liu, Z. Zhao, F. Hu, H. Dai, Construction of a Z-scheme $\text{g-C}_3\text{N}_4/\text{NBGO}/\text{BiVO}_4$ heterostructure with visible-light driven photocatalytic degradation of tetracycline: efficiency, reaction pathway and mechanism, *Catal. Sci. Technol.* 12 (2022) 1339–1358.
- [68] F. Hu, W. Luo, C. Liu, H. Dai, X. Xu, Q. Yue, L. Xu, G. Xu, Y. Jian, X. Peng, Fabrication of graphitic carbon nitride functionalized $\text{P-CoFe}_2\text{O}_4$ for the removal of tetracycline under visible light: optimization, degradation pathways and mechanism evaluation, *Chemosphere* 274 (2021), 129783.
- [69] X. Wang, M. He, Z. Nan, Effects of adsorption capacity and activity site on Fenton-like catalytic performance for Na and Fe co-doped $\text{g-C}_3\text{N}_4$, *Sep. Purif. Technol.* 256 (2021), 117765.
- [70] K. Li, Y. Liang, H. Yang, S. An, H. Shi, C. Song, X. Guo, New insight into the mechanism of enhanced photo-Fenton reaction efficiency for Fe-doped semiconductors: a case study of $\text{Fe/g-C}_3\text{N}_4$, *Catal. Today* 371 (2021) 58–63.
- [71] H. Dong, N. Song, M. Yang, H. Wu, C. Ma, Y. Wang, Fabrication of $\text{HRP/Bi}_2\text{WO}_6$ photoenzyme-coupled artificial catalytic system for efficiently degrading bisphenol A, *Chin. Chem. Lett.* 32 (2021) 2047–2051.
- [72] M. Wang, G. Tan, D. Zhang, B. Li, L. Lv, Y. Wang, H. Ren, X. Zhang, A. Xia, Y. Liu, Defect-mediated Z-scheme $\text{BiO}_{2-x}/\text{Bi}_2\text{O}_{2.75}$ photocatalyst for full spectrum solar-driven organic dyes degradation, *Appl. Catal. B* 254 (2019) 98–112.
- [73] S. Huang, F. Tian, J. Dai, X. Tian, G. Li, Y. Liu, Z. Chen, R. Chen, Highly efficient degradation of chlorophenol over bismuth oxides upon near-infrared irradiation: Unraveling the effect of Bi-O-Bi-O defects cluster and $^1\text{O}_2$ involved process, *Appl. Catal. B* 298 (2021), 120576.
- [74] H. Wang, D. Yong, S. Chen, S. Jiang, X. Zhang, W. Shao, Q. Zhang, W. Yan, B. Pan, Y. Xie, Oxygen-Vacancy-Mediated Exciton Dissociation in BiOBr for Boosting Charge-Carrier-Involved Molecular Oxygen Activation, *J. Am. Chem. Soc.* 140 (2018) 1760–1766.
- [75] J. Guo, H. Jia, A. Zhang, Z. Pei, M. Luo, J. Xue, Q. Shen, X. Liu, B. Xu, MIL-100 (Fe) with mix-valence coordinatively unsaturated metal site as Fenton-like catalyst for efficiently removing tetracycline hydrochloride: Boosting Fe(III)/Fe(II) cycle by photoreduction, *Sep. Purif. Technol.* 262 (2021), 118334.
- [76] S. Shao, G. Wang, Z. Gong, M. Wang, J. Hu, J. Peng, K. Lu, S. Gao, Insights into the role of hydroxyl group on carboxyl-modified MWCNTs in accelerating atenolol removal by $\text{Fe(III)/H}_2\text{O}_2$ system, *Chem. Eng. J.* 425 (2021), 130581.
- [77] Y. Pan, X. Hu, M. Bao, F. Li, Y. Li, J. Lu, Fabrication of MIL-Fe (53)/modified $\text{g-C}_3\text{N}_4$ photocatalyst synergy H_2O_2 for degradation of tetracycline, *Sep. Purif. Technol.* 279 (2021), 119661.
- [78] X. Li, Z. Zeng, G. Zeng, D. Wang, R. Xiao, Y. Wang, C. Zhou, H. Yi, S. Ye, Y. Yang, W. Xiong, A "bottle-around-ship" like method synthesized yolk-shell $\text{Ag}_3\text{PO}_4/\text{MIL-53(Fe)}$ Z-scheme photocatalysts for enhanced tetracycline removal, *J. Colloid Interface Sci.* 561 (2020) 501–511.
- [79] J. Wang, D. Zhi, H. Zhou, X. He, D. Zhang, Evaluating tetracycline degradation pathway and intermediate toxicity during the electrochemical oxidation over a $\text{Ti}/\text{Ti}_4\text{O}_7$ anode, *Water Res.* 137 (2018) 324–334.
- [80] M. Nie, Y. Li, L. Li, J. He, P. Hong, K. Zhang, X. Cai, L. Kong, J. Liu, Ultrathin iron-cobalt oxide nanosheets with enhanced H_2O_2 activation performance for efficient degradation of tetracycline, *Appl. Surf. Sci.* 535 (2021), 147655.
- [81] Z. Li, C. Guo, J. Lyu, Z. Hu, M. Ge, Tetracycline degradation by persulfate activated with magnetic $\text{Cu/CuFe}_2\text{O}_4$ composite: efficiency, stability, mechanism and degradation pathway, *J. Hazard. Mater.* 373 (2019) 85–96.
- [82] X. Jiang, Y. Guo, L. Zhang, W. Jiang, R. Xie, Catalytic degradation of tetracycline hydrochloride by persulfate activated with nano Fe^0 immobilized mesoporous carbon, *Chem. Eng. J.* 341 (2018) 392–401.
- [83] D. Huang, Q. Zhang, C. Zhang, R. Wang, R. Deng, H. Luo, T. Li, J. Li, S. Chen, C. Liu, Mn doped magnetic biochar as persulfate activator for the degradation of tetracycline, *Chem. Eng. J.* 391 (2020), 123532.
- [84] Z. Cai, X. Hao, X. Sun, P. Du, W. Liu, J. Fu, Highly active $\text{WO}_3/\text{anatase-SiO}_2$ aerogel for solar-light-driven phenanthrene degradation: mechanism insight and toxicity assessment, *Water Res.* 162 (2019) 369–382.
- [85] L. Chen, H. Ji, J. Qi, T. Huang, C.-C. Wang, W. Liu, Degradation of acetaminophen by activated peroxymonosulfate using Co(OH)_2 hollow microsphere supported titanate nanotubes: insights into sulfate radical production pathway through CoOH^+ activation, *Chem. Eng. J.* 406 (2021), 126877.
- [86] M. Ahmad, S. Chen, F. Ye, X. Quan, S. Afzal, H. Yu, X. Zhao, Efficient photo-Fenton activity in mesoporous MIL-100(Fe) decorated with ZnO nanosphere for pollutants degradation, *Appl. Catal. B* 245 (2019) 428–438.
- [87] S. Li, J. Hu, Photolytic and photocatalytic degradation of tetracycline: effect of humic acid on degradation kinetics and mechanisms, *J. Hazard. Mater.* 318 (2016) 134–144.
- [88] Y. Xu, H. Lin, Y. Li, H. Zhang, The mechanism and efficiency of MnO_2 activated persulfate process coupled with electrolysis, *Sci. Total Environ.* 609 (2017) 644–654.
- [89] T. Zhao, M. Zheng, C. Fu, G. Li, Y. Xiong, W. Qiu, T. Zhang, J. Zhang, C. Zheng, Effect of low-level H_2O_2 and Fe(II) on the UV treatment of tetracycline antibiotics and the toxicity of reaction solutions to zebrafish embryos, *Chem. Eng. J.* 394 (2020), 125021.